

DISCREPANT MASS ESTIMATES IN THE CLUSTER OF GALAXIES ABELL 1689

E.-H. PENG¹, K. ANDERSSON¹, M. W. BAUTZ¹, G. P. GARMIRE²

ACCEPTED TO APJ: *June 20, 2009*

ABSTRACT

We present a new mass estimate of a well-studied gravitational lensing cluster, Abell 1689, from deep *Chandra* observations with a total exposure of 200 ks. Within $r = 200 h^{-1}\text{kpc}$, the X-ray mass estimate is systematically lower than that of lensing by 30-50%. At $r > 200 h^{-1}\text{kpc}$, the mass density profiles from X-ray and weak lensing methods give consistent results. The most recent weak lensing work suggest a steeper profile than what is found from the X-ray analysis, while still in agreement with the mass at large radii. Fitting the total mass profile to a Navarro-Frenk-White model, we find $M_{200} = (1.16^{+0.45}_{-0.27}) \times 10^{15} h^{-1} M_{\odot}$ with a concentration, $c_{200} = 5.3^{+1.3}_{-1.2}$, using non-parametric mass modeling. With parametric profile modeling we find $M_{200} = (0.94^{+0.11}_{-0.06}) \times 10^{15} h^{-1} M_{\odot}$ and $c_{200} = 6.6^{+0.4}_{-0.4}$. This is much lower compared to masses deduced from the combined strong and weak lensing analysis. Previous studies have suggested that cooler small-scale structures can bias X-ray temperature measurements or that the northern part of the cluster is disturbed. We find these scenarios unlikely to resolve the central mass discrepancy since the former requires 70-90% of the space to be occupied by these cool structures and excluding the northern substructure does not significantly affect the total mass profiles. A more plausible explanation is a projection effect. Assuming that the gas temperature and density profiles have a prolate symmetry, we can bring the X-ray mass estimate into a closer agreement with that of lensing. We also find that the previously reported high hard-band to broad-band temperature ratio in A1689, and many other clusters observed with *Chandra*, may be resulting from the instrumental absorption that decreases 10-15% of the effective area at ~ 1.75 keV. Caution must be taken when analyzing multiple spectral components under this calibration uncertainty.

Subject headings: galaxies: clusters: individual: Abell 1689 — X-rays: galaxies: clusters

1. INTRODUCTION

Abell 1689 is a massive galaxy cluster with the largest known Einstein radius to date, $\theta_E = 45''$ for $z_s = 1$ (e.g., Tyson et al. 1990; Miralda-Escude & Babul 1995; Broadhurst et al. 2005a,b), located at a moderately low redshift of $z = 0.187$ (Frye et al. 2007). It has a regular X-ray morphology, indicating that the cluster is likely in hydrostatic equilibrium, but the mass derived from the X-ray measurement is often a factor of 2 or more lower than that from gravitational lensing at most radii. Using *XMM-Newton* observations, Andersson & Madejski (2004, A04 hereafter) find an asymmetric temperature distribution and a high redshift structure in A1689, providing evidence for an ongoing merger in this cluster.

Saha et al. (2007) confirm the existence of substructures, using different sets of lensed images. This is also seen in other lensing work (e.g., Broadhurst et al. 2005a; Diego et al. 2005; Zekser et al. 2006; Halkola et al. 2006; Limousin et al. 2007). Though these clumps are clearly identified, they only contribute $\simeq 7\%$ of the total mass within $250 h^{-1}\text{kpc}$ and are likely to be line-of-sight filaments rather than distinct merging groups. Furthermore, Lokas et al. (2006) used the redshift distribution of galaxies to conclude that A1689 is probably surrounded by a few structures superposed along the line of sight that do not interact with the cluster dynamically, but would

affect lensing mass estimates.

A recent joint *Chandra*, HST/ACS, and Subaru/Suprime cam analysis by Lemze et al. (2008a, L08 hereafter) suggested that the temperature of A1689 could be as high as $T = 18$ keV at $100 h^{-1}\text{kpc}$, almost twice as large as the observed value at that radius. The derived 3D temperature profile was based on the X-ray surface brightness, the lensing shear, and the assumption of hydrostatic equilibrium. From the disagreement between the observed X-ray temperature and the deduced one, L08 concluded that denser, colder, and more luminous small-scale structures could bias the X-ray temperature.

In another study of 192 clusters of galaxies from the *Chandra* archive, Cavagnolo et al. (2008) find a very high hard-band ($2/(1+z)$ -7 keV) to broad-band (0.7-7 keV) temperature ratio for A1689, $1.36^{+0.14}_{-0.12}$ compared to 1.16 ± 0.10 for the whole sample. They also find that merging clusters tend to have a higher temperature ratio, as predicted by Mathiesen & Evrard (2001) where this high ratio is attributed to accreting cool subclusters lowering the broad-band temperature by contributing large amounts of line emission in the soft band. The hard-band temperature, however, should be unaltered by this emission. The simulations of Mathiesen & Evrard (2001) show an increase of temperature ratios of $\sim 20\%$ in general, which is close to the average of the sample of Cavagnolo et al. (2008), 16%.

A recent study, using the latest *Chandra* data (Riemer-Sørensen et al. 2009) claim that the cluster harbors a cool core and thus is relaxed based on a hardness-ratio map

Electronic address: epeng@mit.edu

¹ MKI, Massachusetts Institute of Technology, Cambridge, MA 02139, USA

² Department of Astronomy and Astrophysics, Pennsylvania State University, PA 16802, USA

analysis. They further calculate a mass profile from the X-ray data and conclude that the X-ray and lensing measurements are in good agreement when the substructure to the NE is excluded.

In this work, we examine the possibility of an extra spectral component in the X-ray data and derive an improved gravitational mass profile, including a recent 150 ks *Chandra* observation. §2 describes the details of data reduction and examines the possibility of an uncorrected absorption edge in the data. In §3, we explore the physical properties of the potential cool substructures under a two-temperature (2T) model and examine if they can be used to explain the high hard-band to broad-band temperature ratio. In §4, assuming that the temperature profile derived by L08 is real, we investigate what this implies for the required additional cool component. In §5, we derive the mass profile under both one and two temperature-phase assumptions, using both parametric and non-parametric methods. Finally, we discuss our results in §6 and summarize in §7.

Throughout this paper, we assume $H_0 = 100 h^{-1} \text{ km s}^{-1} \text{ Mpc}^{-1}$, $\Omega_m = 0.3$, and $\Omega_\lambda = 0.7$, which gives $1'' = 2.19 h^{-1} \text{ kpc}$ at the cluster redshift of 0.187 (Frye et al. 2007). Abundances are relative to the photospheric solar abundances of Anders & Grevesse (1989). All errors are 1σ unless otherwise stated.

2. DATA REDUCTION

2.1. *Chandra*

Chandra data were processed through CIAO 4.0.1 with CALDB 3.4.3. Since all of the observations had gone through Repro III in the archive, reprocessing data was not needed. Updated charge-transfer inefficiency and time-dependent gain corrections had already been applied. For data taken in VFaint telemetry mode, additional screening to reject particle background was used. Events with bad CCD columns and bad grades were removed. Lightcurves were extracted from four I-chips with cluster core and point sources masked in the 0.3-12 keV band and filtered by *lc_clean* which used 3σ clipping and a cut at 20% above the mean. Finally, *make_readout_bg* were used to generate Out-of-Time event file. These events were multiplied by 1.3% and subtracted from the images or the spectra to correct readout artifacts. For spectral analysis, emission-weighted response matrices and effective area files were constructed for each spectral region by *mkacisrmf* and *mkwarf*.

2.2. Background Subtraction and Modeling

Blank-field data sets³ were used to estimate the background level. After reprojecting the blank-sky data sets onto the cluster’s sky position, the background was scaled by the count rate ratio between the data and the blank-field background in the 9.5-12 keV band to account for the variation of particle induced background. Below 1 keV, the spatial varying galactic ISM emission (Markevitch et al. 2003) could cause a mismatch between the real background and the blank-field data. By analysing the spectra in the same field but sufficiently far from the cluster, tailoring this soft component can be made using

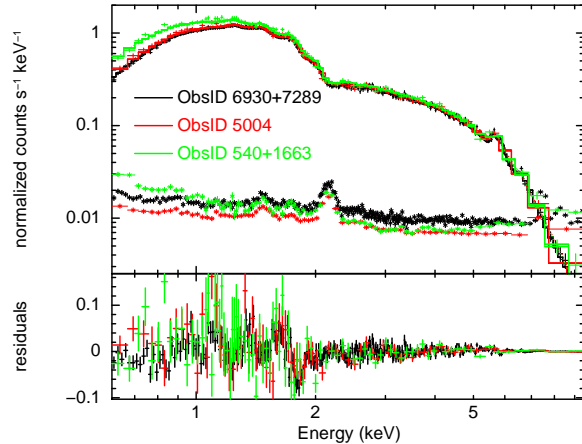


FIG. 1.— The 0.6-9.5 keV *Chandra* spectrum of A1689 from the central $3'$ region. The upper panel shows the data, plotted against an absorbed VAPEC model (solid line) with each element’s abundance and absorption column density as free parameters. The lower panel shows residuals.

an unabsorbed $T \sim 0.2$ keV, solar abundance thermal model (Vikhlinin et al. 2005).

The current available blank-sky data were created from observations before 2005. As the solar cycle gradually reaches its minimum, the particle induced background increases. Therefore, newer observations need a much higher background normalization with a factor of 1.2-1.3. This leads an overestimate of the background in the soft band because other components like cosmic X-ray background (CXB) does not change as the particle induced background does. To correct the over-subtracted CXB and halo emission, an absorbed power law with photon index fixed at 1.4 (De Luca & Molendi 2004) plus an unabsorbed thermal model was used to fit the blank-field background subtracted spectrum taken at $r > 13'$.

The background normalization factors used for each observation are listed in Table 1

2.3. *XMM-Newton*

The data from two MOS detectors were processed with the XMM-SAS 6.1.0 tool, *emchain*. Background flares were removed by a double-filtering method (Nevalainen et al. 2005) from $E > 10$ keV and 1-5 keV light curves. Only events with pixel PATTERNS 0-12 were selected. Since *XMM* data were only used to crosscheck the result of the multi-component analysis of *Chandra* spectra, extracted from the central region where background modeling is relatively unimportant, we used the simpler local background, taken from $6'-8'$. Spectral response files were created by *rmfgen* and *arfgen*. We did not include PN data because the measured mean redshift, 0.169 ± 0.001 , was not consistent with those from *XMM* MOS or *Chandra* data. This could indicate a possible gain offset for PN detector, although A04 did not find any evidence for that.

2.4. Systematic Uncertainties

L08 pointed out some issues about previous *Chandra* observations (ObsID 540, 1663, and 5004). The column density from *Chandra* data is much lower than the Galactic value, $1.8 \times 10^{20} \text{ cm}^{-2}$ (Dickey & Lockman 1990),

³ http://asc.harvard.edu/cal/Acis/Cal_prods/bkgrnd/acisbg.

TABLE 1
Chandra OBSERVATION LOG

ObsID	Data Mode	Obs. Date	Exposure (ks)	Background Normalization			
				I0	I1	I2	I3
540	FAINT	2000-04-15	10.3	1.06	1.09	1.03	1.11
1663	FAINT	2001-01-07	10.7	1.00	0.98	0.99	1.04
5004	VFAINT	2004-02-28	19.9	0.93	0.89	0.89	0.94
6930	VFAINT	2006-03-06	75.9	1.21	1.18	1.18	1.28
7289	VFAINT	2006-03-09	74.6	1.19	1.20	1.19	1.27

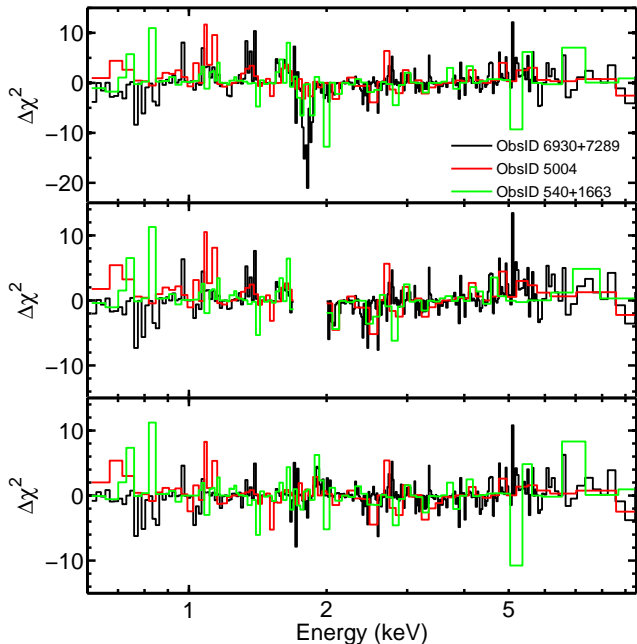


FIG. 2.— Fit residuals, showing each channel’s contribution to the total χ^2 . *Top*: an absorbed VAPEC model fit to central $3'$ spectrum. *Middle*: same as the above, ignoring data in 1.7-2 keV. *Bottom*: adding an absorption edge with $E_{thresh} = 1.77$ keV and $\tau = 0.12$.

which is also supported by the ROSAT data (Andersson & Madejski 2004). The temperature difference can be as high as 1.3 keV depending on the choice of column density. In the high energy band, the data is systematically higher than the model prediction. With two long *Chandra* observations, ObsID 6930 and 7289, we clearly see an unusual feature in the datasets which may give clues to problems mentioned before. Fig. 1 shows an absorbed APEC model (Smith et al. 2001) fit to the central $3'$ spectrum. The prominent residual at ~ 1.75 keV is present in all of our observations and appeared as the biggest contributor to the total χ^2 (See Fig. 2). This residual can not be eliminated by adjusting individual abundances in the cluster or in the absorbing column (the cluster is at high galactic latitude). Because the residual around 1.75 keV is an order of magnitude larger than the background, it is not likely related to the background subtraction. In addition to this absorption, the residuals are systematically rising with the energy from negative to positive values. This trend is not changed when fitting the spectrum with data between 1.7-2.0 keV excluded (Fig. 2). We found that multiplying a XSPEC Edge model can correct the residual at ~ 1.75 keV, remove steadily rising residuals with the energy, and make the column density agree with the Galactic value.

 TABLE 2
 ABSORPTION EDGE PARAMETERS

Model	fit range	E_{thresh} (keV)	τ
1T	$2.5' \times 2.5'$	$1.75^{+0.01}_{-0.01}$	$0.15^{+0.01}_{-0.01}$
1T	$r < 3'$	$1.74^{+0.01}_{-0.01}$	$0.14^{+0.01}_{-0.01}$
1T	$r < 3'$, ignore 1.75-1.85 keV	$1.76^{+0.03}_{-0.02}$	$0.13^{+0.01}_{-0.01}$
2T ^a	$r < 3'$, ignore 1.75-1.85 keV	$1.76^{+0.02}_{-0.02}$	$0.12^{+0.01}_{-0.01}$
1T+PL ^b	$r < 3'$, ignore 1.75-1.85 keV	$1.76^{+0.03}_{-0.02}$	$0.11^{+0.01}_{-0.01}$
1T	$0.2' < r < 3'$	$1.74^{+0.01}_{-0.01}$	$0.14^{+0.01}_{-0.01}$
1T	$0.2' < r < 3'$, ignore 1.75-1.85 keV	$1.90^{+0.04}_{-0.06}$	$0.12^{+0.01}_{-0.01}$

^a $T_1 = 8.0^{+0.5}_{-0.5}$ keV, $T_2 = 34^{+12}_{-6}$ keV.

^b $T_1 = 9.3^{+0.3}_{-0.4}$ keV, $\Gamma = -0.7^{+0.3}_{-0.4}$.

Since the spectrum was extracted from a very large region, we averaged the position-dependent response matrices and effective area functions by the number of counts at each location. It is possible that the absorption feature is caused by improper weighting of those response files, or that this peculiarity only exists at certain regions. To dispel those doubts, we separated the central $2.5' \times 2.5'$ area into 12 square regions and simultaneously fit these spectra with one spectral model (We only used data from ObsID 6930 and 7289 to simplify the fitting procedure). All parameters, except for the normalization, were tied together. The residuals from the single temperature fit are shown in Fig. 3. Although the fit is now acceptable with a $\chi^2/dof = 3448.8/3387$, the residuals still show the same systematic trend as seen in the composite spectrum, and the column density, $(1.0^{+0.4}_{-0.4}) \times 10^{20}$ cm⁻² (90% confidence level), appears low. When adding an absorption edge to the single temperature model, the derived parameters of this edge, $E_{thresh} = 1.75^{+0.01}_{-0.01}$ keV and $\tau = 0.15^{+0.01}_{-0.01}$, are consistent with results from the integrated spectrum. In fact, E_{thresh} and τ do not strongly depend on how we model the cluster spectrum. We list fitted values of E_{thresh} and τ from different cluster models and spectral extraction regions in Table 2. Similar values are also found in other *Chandra* datasets (see the Appendix).

The low column density can be explained by the absorption at ~ 1.75 keV. This absorption has to be something like an edge, which affects the wide energy range of the spectrum, rather than an absorption line that influences only a limited energy range. The consequence to the fit resulting from this absorption is that the overall spectral normalization decreases. Since less soft photons are produced from the model, the heavy absorption by the foreground is no longer needed. We quantified the above statement in Table 3 in which we simulated 100 single temperature spectra with an absorption edge at

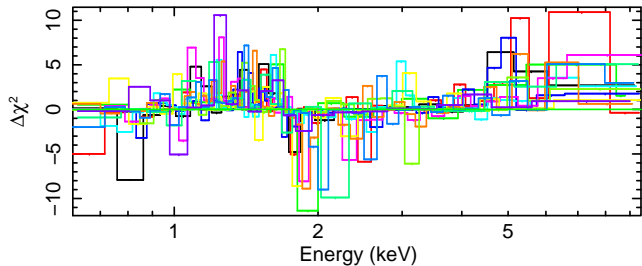


FIG. 3.— Residuals from an absorbed APEC model fit to 12 spectra extracted from central $2.5' \times 2.5'$ region of ObsID 6930 and 7289. We simultaneously fit these spectra and tied all parameters, except the normalization, together.

$E_{\text{thresh}} = 1.74$ keV and $\tau = 0.14$, fit with a single temperature (1T) model, and compared with the observations. The spectral normalization is increasing with rising column density as we exclude more data around 1.75 keV. Meanwhile, the cluster temperature and abundance are slightly decreasing. The changes of those parameters from different bandpass used in the fitting match perfectly to what are seen in the real data.

The CCD calibration around the Si-edge for ACIS-I detectors is a known issue (N. Schulz, private communication). However, it is unknown whether a correction like an edge model is needed, or if we should simply ignore the data around the Si edge. If the former is true, results from the multiple-component analysis or the hard-band/broad-band temperature measurement without applying this edge model beforehand are very questionable. As seen in Table 3, including the edge model can make the hard-band temperature 30% hotter than the that of the broad-band. This temperature ratio depends on the cluster temperature and the quality of the data. On the other hand, if the latter is true, the spectrum implies that an additional component which is much harder than 10 keV emission is definitely required. Though, the fit is not as good as that with an edge model. From the fact that the absorption depth is sufficiently far from the zero, even if we exclude data around 1.75 keV (Table 2), the intensity jump around this energy indeed exists.

A1689 is a very hot cluster that unfortunately will be seriously affected by the calibration uncertainty around the Si edge if that can be modeled by something similar to an edge model. Lacking the knowledge that correctly treats the systematic residuals seen in the data, we provide both models, applying an absorption edge or simply ignoring the data around 1.75 keV, as our best guess to the thermal state of this cluster.

2.5. Spectral fitting

Spectra were fit with XSPEC 12.3.1 package (Arnaud 1996). We adopted χ^2 statistic and grouped the spectra to have a minimum of 25 counts per bin. However, when fitting background dominated spectra, χ^2 statistic is proven to give biased temperature (Leccardi & Molendi 2007). Another choice available in XSPEC is using Cash statistic with modeled, rather than subtracted background. Since modeling the background needs many components: cosmic ray induced background (broken power-laws plus several Gaussians), particle background (broken power-laws), cosmic X-ray background (power-law), galactic emission (thermal), etc, the whole spectral

model will be very complicated for analysis like deprojection, which simultaneously fits all of the spectra extracted at different radii. We decided to use χ^2 statistic but with a different grouping method to bypass the difficulty in background modeling.

As shown in Table 4, we simulated 500 *Chandra* spectra with $N_H = 1.8 \times 10^{20}$ cm $^{-2}$, $Z = 0.2$ solar, and $T = 9, 7, 5$ keV with Norm $^4 = 1.51 \times 10^4, 1.52 \times 10^4, 1.56 \times 10^4$, respectively. The spectral normalization was chosen to match the observed flux at $r = 6.5' - 8.8'$, where the background is $\sim 90\%$ of the source in 0.9-7.0 keV band. Spectra were generated based on the response files of ObsID 6930 and 7289 with a total exposure time of 150 ks. When data are binned to have a minimum of 25 total counts (background included) per channel, a 9 keV gas will be measured to be 5 keV. Raising the threshold can lessen this bias. However, even with 400 counts per bin, which greatly reduces the spectral resolution by a factor of 10, the temperature is still being underestimated by ~ 1 keV for $T = 9$ keV gas. We found out that binning data to have at least 2 counts above the background can recover the true temperature, though this minimum have to be adjusted according to the background contribution. Spectra at large radii were binned by this grouping scheme.

3. SPECTRAL ANALYSIS

3.1. Single temperature model

We first determined the general properties of the cluster, using the spectrum extracted from the central $3'$ (395 h $^{-1}$ kpc) region and fitting it with a single temperature VAPEC model. The Ne, Mg, Si, S, Ar, Ca, Fe, Ni abundances and the redshift were free to vary. The column density was fixed at the Galactic value. The best-fit parameters are listed in Table 5. For *Chandra* data we fixed the Si abundance at $0.4 Z_{\odot}$, since the residual at 1.75 keV (§2.4) was close to Si XIV $K\alpha$ line (2.01 keV, rest-frame).

Table 5 shows that a single-temperature model is moderately adequate for *XMM-Newton* MOS data but not for *Chandra* when the absorption edge is not modeled. In addition to this difference, the *Chandra* temperature is ~ 1 keV higher than that of *XMM-Newton*. This temperature disagreement is likely related to the cross-calibration problems, as noted in other studies (e.g., Kotov & Vikhlinin 2005; Vikhlinin et al. 2006; Snowden et al. 2008, L. David 5), but it could also be caused by incorrect cluster modeling. A two-temperature model will be investigated in §3.2.

Chandra data also have a higher Fe and a much higher Ni abundance, resulting an unusually high Ni/Fe ratio of 7.5 ± 1.3 and 9.0 ± 1.2 Ni $_{\odot}$ /Fe $_{\odot}$ with and without an absorption edge correction, respectively, in contrast to the *XMM-Newton* value of 1.8 ± 1.6 Ni $_{\odot}$ /Fe $_{\odot}$. Our *XMM-Newton* MOS result is in agreement with that of de Plaa et al. (2007), 0.9 ± 1.5 Ni $_{\odot}$ /Fe $_{\odot}$, obtained from MOS and PN spectra from the $r < 1.3'$ region with a differential emission measure MEKAL-based model, *wdem* (Kaastra et al. 2004). Such a high Ni/Fe ratio greatly

4 Spectral normalization, Norm = $\frac{10^{-14}}{4\pi((1+z)D_A)^2} \int n_e n_H dV$, where n_e and n_H are in cm $^{-3}$, V in cm 3 , and D_A in cm.

5 http://cxc.harvard.edu/ccw/proceedings/07_proc/presentations/david

TABLE 3
 SUMMARY OF $r < 3'$ SPECTRAL FITS AND 1T SIMULATIONS

fit range	Chandra observations				χ^2/dof	Simulated 200 ks spectra ^a			
	T (keV)	Z (Z_\odot)	N_H (10^{20}cm^{-2})	Norm (10^{-2})		T (keV)	Z (Z_\odot)	N_H (10^{20}cm^{-2})	Norm (10^{-2})
0.6-9.5 keV ^b	$10.5^{+0.1}_{-0.1}$	$0.36^{+0.02}_{-0.02}$	$1.9^{+0.2}_{-0.2}$	$1.920^{+0.007}_{-0.007}$	1591/1390	$10.4^{+0.1}_{-0.1}$	$0.36^{+0.02}_{-0.02}$	$1.9^{+0.1}_{-0.2}$	$1.899^{+0.008}_{-0.006}$
0.6-9.5 keV	$10.7^{+0.4}_{-0.1}$	$0.41^{+0.02}_{-0.02}$	$0.7^{+0.2}_{-0.2}$	$1.841^{+0.007}_{-0.007}$	1867/1390	$10.6^{+0.1}_{-0.1}$	$0.40^{+0.02}_{-0.02}$	$0.6^{+0.1}_{-0.2}$	$1.820^{+0.008}_{-0.007}$
ignore 1.75-1.85 keV	$10.6^{+0.1}_{-0.1}$	$0.40^{+0.02}_{-0.02}$	$0.9^{+0.2}_{-0.2}$	$1.857^{+0.007}_{-0.007}$	1743/1366	$10.5^{+0.1}_{-0.1}$	$0.39^{+0.02}_{-0.02}$	$0.8^{+0.1}_{-0.1}$	$1.833^{+0.008}_{-0.006}$
ignore 1.7-2.0 keV	$10.5^{+0.1}_{-0.1}$	$0.39^{+0.02}_{-0.02}$	$1.1^{+0.2}_{-0.2}$	$1.868^{+0.008}_{-0.008}$	1645/1327	$10.3^{+0.1}_{-0.1}$	$0.38^{+0.02}_{-0.02}$	$1.2^{+0.2}_{-0.1}$	$1.852^{+0.008}_{-0.007}$
ignore 1.7-2.5 keV	$10.4^{+0.1}_{-0.1}$	$0.38^{+0.02}_{-0.02}$	$1.6^{+0.2}_{-0.2}$	$1.892^{+0.008}_{-0.008}$	1466/1222	$10.2^{+0.1}_{-0.1}$	$0.37^{+0.02}_{-0.01}$	$1.6^{+0.2}_{-0.2}$	$1.877^{+0.007}_{-0.008}$
ignore 1.7-3.0 keV	$10.4^{+0.1}_{-0.1}$	$0.37^{+0.02}_{-0.02}$	$1.8^{+0.2}_{-0.2}$	$1.904^{+0.009}_{-0.009}$	1317/1120	$10.2^{+0.1}_{-0.1}$	$0.36^{+0.02}_{-0.01}$	$1.7^{+0.2}_{-0.2}$	$1.886^{+0.008}_{-0.009}$
1.7-7.0 keV	$13.1^{+0.3}_{-0.3}$	$0.44^{+0.02}_{-0.02}$	1.8	$1.817^{+0.008}_{-0.008}$	1100/960	$12.7^{+0.3}_{-0.3}$	$0.44^{+0.02}_{-0.02}$	1.8	$1.790^{+0.008}_{-0.008}$
0.7-7.0 keV	$10.1^{+0.1}_{-0.1}$	$0.40^{+0.02}_{-0.02}$	1.8	$1.867^{+0.006}_{-0.006}$	1655/1164	$10.0^{+0.1}_{-0.1}$	$0.39^{+0.02}_{-0.02}$	1.8	$1.849^{+0.005}_{-0.006}$

NOTE. — Errors are 1σ or 68% CL for 100 simulations.

^a The absorption edge is at $E_{\text{thresh}} = 1.74$ keV with $\tau = 0.14$. We used $T = 10.5$ keV, $Z = 0.36 Z_\odot$, $z = 0.187$, Norm = 1.9×10^{-2} (corresponding to $S_{X[0.6-9.5\text{keV}]} = 2.4 \times 10^{-11}$ erg cm $^{-2}$ s $^{-1}$), $N_H = 1.8 \times 10^{20}$ cm $^{-2}$.

^b Multiplied by an absorption edge at $E_{\text{thresh}} = 1.74$ keV with $\tau = 0.14$.

 TABLE 4
 SUMMARY OF 1T SIMULATIONS OF 150 KS *Chandra*
 SPECTRA AT $r = 6.5'-8.8'$.

Min counts (1)	T_0 (keV) (2)	T_{med} (keV) (3)	dof_{mean} (4)
25 (tot)	9	$4.9^{+2.1}_{-1.2}$	396
	7	$4.2^{+1.6}_{-1.1}$	396
	5	$3.4^{+0.9}_{-0.7}$	395
100 (tot)	9	$6.8^{+5.1}_{-2.4}$	142
	7	$5.9^{+3.1}_{-1.7}$	142
	5	$4.3^{+1.5}_{-1.1}$	141
400 (tot)	9	$7.9^{+7.2}_{-4.2}$	40
	7	$6.6^{+4.2}_{-2.0}$	40
	5	$4.8^{+1.9}_{-1.3}$	40
2 (net)	9	$8.6^{+7.8}_{-2.7}$	170
	7	$7.2^{+4.7}_{-2.2}$	166
	5	$5.2^{+1.9}_{-1.4}$	155

NOTE. — (1) minimum (total or net) counts per channel, (2) input temperature, (3) median temperature, (4) median dof . Errors are 68% CL for 500 simulations.

exceeds the yield of typical SN Ia models (Iwamoto et al. 1999), which range from 1.4-4.8 Ni $_\odot$ /Fe $_\odot$. Since there is a known temperature discrepancy between *Chandra* and *XMM-Newton* that would affect elemental abundance determinations, direct Fe and Ni line measurements will be conducted in §3.4.

The S abundance, determined mostly by the S XVI K α line at 2.62 keV (rest-frame), should be accurately measured for *XMM-Newton* EPIC since it suffers little systematic uncertainty (Werner et al. 2008). However, without an absorption edge correction, there is basically no S detection for *Chandra* data, which strongly contradicts the *XMM-Newton* result. This shows the great impact of the absorption at 1.75 keV. When including an edge model into the fit, we have consistent S abundances for both instruments.

3.2. Two temperature model

To get some clues to the nature of the claimed cool substructures in A1689, a simple two temperature model was fit to the spectrum extracted from the $r < 3'$ (395

h^{-1} kpc) region where the quality of the data was high enough to test it. We used two absorbed VAPEC models, with variable normalization but linked metallicities between the two phases. The column density was fixed at the Galactic value. To reduce the uncertainty on measuring metallicities, we tied the abundances of α -elements (O, Ne, Mg, Si, S, Ar, and Ca) together and fixed the remaining abundances at the solar value, except for Fe and Ni. Since the hotter phase temperature, T_{hot} , was harder to constrain, it was frozen at a certain value above the best-fit single temperature fit, T_{1T} . We changed this increment from 0.5 to 50 keV to explore the whole parameter space.

Fig. 4 shows the temperature of the cooler gas, T_{cool} , and the fractional contribution of the cooler gas, EM $_{\text{cool}}$ /EM $_{\text{total}}$, as a function of T_{hot} . As T_{hot} increases, T_{cool} and EM $_{\text{cool}}$ /EM $_{\text{total}}$ increase as well. T_{cool} eventually becomes T_{1T} once T_{hot} is greater than 20 keV and very little gas is left in the hot phase, which is also supported by the *XMM-Newton* data. For $T_{\text{hot}} \approx 18$ keV, there has to be 30%, 60% of the cool gas at the temperature of 5, 8 keV inferred from *Chandra* and *XMM-Newton* data, respectively. *Chandra* absorption corrected data show similar results as *XMM-Newton* data do at this temperature. Although there is some inconsistency between *Chandra* and *XMM-Newton* data, both indicate that the cool component, if it indeed exists, is not cool at all. $T = 5$ keV is the typical temperature of a medium sized cluster with a mass of $M_{500} = 2.9 \times 10^{14} h^{-1} M_\odot$ (Vikhlinin et al. 2006).

To quantify how significant the detection of this extra component was, we conducted an F -test from the fits of 1T (the null model) and 2T models. However, because the 2T model reduces to 1T when the normalization of one of the two components hits the parameter space boundary (ie, zero), the assumption of F -test is not satisfied (see Protassov et al. 2002). Therefore, we simulated 1000 1T *Chandra* spectra and performed the same procedure to derive the F -test probability, P_F , based on the F distribution. Fig. 4 shows the distribution of P_F from simulated data at the 68, 90, 95, and 99 percentile overplotted with P_F from *Chandra* and *XMM-Newton* data. We plot P_F in Fig. 4 rather than the F statistic, since P_F is a scaler that does not depend on the degrees

TABLE 5
 BEST-FIT VAPEC PARAMETERS

	T (keV)	z	Ne	Mg	Si	S	Ar	Ca	Fe	Ni	χ^2/dof
Chandra ^a	$10.2^{+0.1}_{-0.1}$	$0.186^{+0.001}_{-0.001}$	$0.59^{+0.32}_{-0.29}$	$1.95^{+0.30}_{-0.30}$	0.4_f	< 0.05	< 0.19	< 0.12	$0.40^{+0.02}_{-0.02}$	$3.60^{+0.44}_{-0.47}$	1664/1360
Chandra ^b	$10.5^{+0.1}_{-0.1}$	$0.186^{+0.001}_{-0.001}$	< 0.18	$1.16^{+0.22}_{-0.42}$	0.4_f	$0.66^{+0.22}_{-0.32}$	< 0.38	< 0.09	$0.37^{+0.01}_{-0.02}$	$2.77^{+0.48}_{-0.45}$	1545/1382
XMM MOS	$9.4^{+0.1}_{-0.1}$	$0.183^{+0.001}_{-0.001}$	$0.35^{+0.40}_{-0.35}$	$1.55^{+0.43}_{-0.40}$	$0.50^{+0.20}_{-0.19}$	$0.64^{+0.23}_{-0.23}$	< 0.57	$1.38^{+0.69}_{-0.71}$	$0.31^{+0.02}_{-0.02}$	$0.57^{+0.49}_{-0.47}$	982/840

NOTE. — Al, O fixed at 0.4 solar and He, C, N at 1 solar. For the elements whose abundances reach the lower bound, zero, only the upper limits are shown. Errors are 1σ .

^a without an absorption edge and ignoring data at 1.75–1.85 keV.

^b with an absorption edge. Edge parameters are determined from the data with $E_{thresh} = 1.74^{+0.01}_{-0.01}$ keV and $\tau = 0.13^{+0.01}_{-0.01}$.

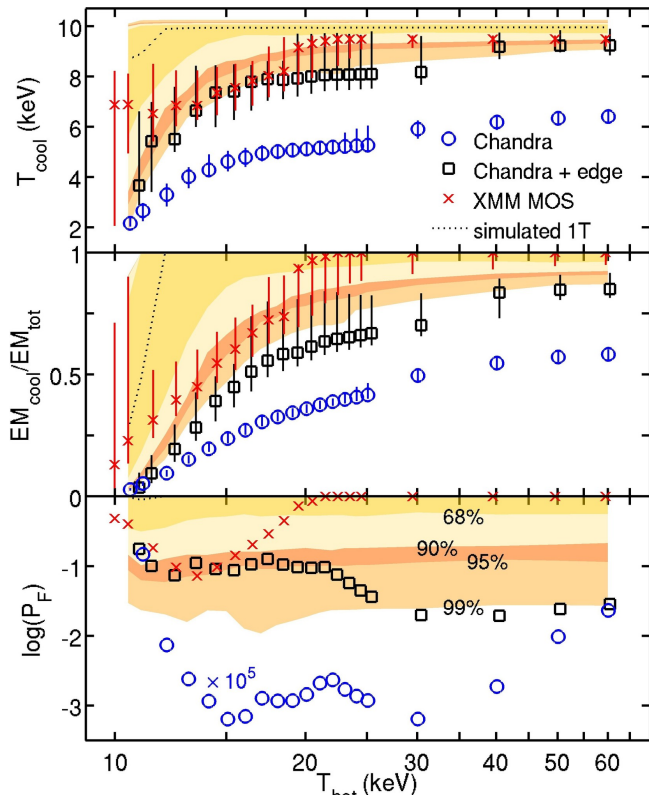


FIG. 4.— The temperature of the cooler gas T_{cool} , the emission measure ratio EM_{cool}/EM_{total} , and the F-test probability P_F are plotted as a function of T_{hot} . The shaded region represents 68%, 90%, 95%, and 99% CL from 1000 simulated $T = 10.1$ keV *Chandra* spectra. The P_F from *Chandra* data without the absorption edge corrected (circles) is multiplied by 10^5 .

of freedom of the fits and is ideal to compare observations that have different data bins. For $T_{hot} < 20$ keV, both the edge-corrected *Chandra* data and the *XMM-Newton* data are within the 95 percentile of the simulated 1T model and we conclude that a 2T model is possible but not necessary to describe the data.

3.3. Hard-band, broad-band temperature

In addition to multiple-component modeling, measuring the temperature in different band-pass is another way to demonstrate the presence of multiple components. Cavagnolo et al. (2008) reported a very high hard-band to broad-band temperature ratio for A1689, $1.36^{+0.14}_{-0.12}$, from analysis of 40 ks of *Chandra* data, suggesting that this could relate to ongoing or recent mergers. Following the convention in Cavagnolo et al. (2008), we fit the spectrum in the 0.7–7.0 keV (broad) and $2.0/(1+z)$ –7.0 keV (hard)

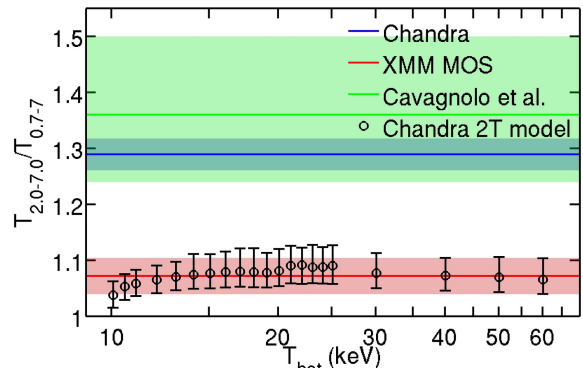


FIG. 5.— The hard-band to broad-band temperature ratio $T_{2.0-7.0}/T_{0.7-7.0}$ of simulated *Chandra* 2T spectra (circles) plotted against T_{hot} . The shaded regions show the observed temperature ratios from *Chandra* and *XMM-Newton* MOS data. Also shown is the temperature ratio from 40 ks *Chandra* data by Cavagnolo et al. (2008).

band with a single-temperature model. In contrast to C08, we do not use the $r < R_{2500}$ region with the core excised, but simply take the spectrum from the whole central $3'$ ($395 h^{-1} \text{kpc}$) region. The hard-band to broad-band temperature ratio from *Chandra* data, 1.29 ± 0.03 , strongly disagrees with that of *XMM MOS*, 1.07 ± 0.03 . This result is anticipated since an absorption edge feature found in the *Chandra* spectrum (§2.4) is close to the cut-off of the hard band. After correcting for this absorption, the temperature ratio is in the range of 1 to 1.08 for an absorption depth of $\tau = 0.14 - 0.10$. As a consistency check, we simulated spectra according to the best-fit 2T models (from *Chandra* data) from §3.2 to see whether these models can explain such a high temperature ratio. Results are plotted in Fig. 5. None of the 2T models can reproduce the observed ratio of the uncorrected *Chandra* data. Thus we conclude that there is no evidence from this ratio of the presence of multiple components or merging activity. Furthermore, Leccardi & Molendi (2008) do not find any discrepancy between the hard band (2–10 keV) and broad band (0.7–10 keV) temperature profiles, except for $r < 0.05 r_{180}$, for a sample of ~ 50 hot, intermediate redshift clusters based on *XMM-Newton* observations. The high hard-band to broad-band temperature ratio seen in A1689, as well as in many other clusters observed with *Chandra* (Cavagnolo et al. 2008), might be due to the aforementioned calibration uncertainty.

3.4. Emission line diagnostics

When fitting the whole spectrum, the temperature is mainly determined by the continuum due to the low

TABLE 6

Line	Energy (keV)	Centroid ^a (keV)	Width ^a (eV)
Fe xxv K α	6.636, 6.668, 6.682, 6.700	6.686	23
Fe xxv K β	7.881	7.877	19
Fe 8.3 keV ^b	8.246, 8.252, 8.293, 8.486	8.282	68
Fe xxvi K α	6.952, 6.973	6.964	14
Fe 8.7 keV ^c	8.698, 8.701, 8.907, 8.909	8.764	97
Ni xxvii K α	7.765, 7.805	7.793	19
Ni xxviii K α	8.074, 8.101	8.090	16

^a Emissivity-weighted center and one standard deviation. The line emissivity is calculated at $T = 10$ keV from *Chandra* ATOMDB 1.3.1.

^b including Fe xxvi K β , xxv K γ , and xxv K δ .

^c including Fe xxvi K δ and xxvi K γ .

amount of line emission at the temperature of A1689. In order to extract the emission line information, which can provide an additional temperature diagnostic, we fit the 4.5-9.5 keV spectrum with an absorbed thermal bremsstrahlung model plus Gaussians. There are 42 lines whose emissivity is greater than 10^{-19} photons $\text{cm}^{-3}\text{s}^{-1}$ at $kT = 10$ keV from ions of Fe xxv, Fe xxvi, Ni xxvii, Ni xxviii, according to *Chandra* ATOMDB 1.3.1. Considering the CCD energy resolution, we grouped those lines into seven Gaussians and used the emissivity-weighted centroid and one standard deviation as the line center and width, respectively. The Ni xxvii K α line is ~ 80 eV away from the Fe xxv K β line, not separable under CCD resolution unless we have extremely good data quality. Since we obtained an unusually high Ni/Fe ratio of $\sim 9 \text{ Ni}_{\odot}/\text{Fe}_{\odot}$ from a VAPEC model fit to the whole spectrum (§3.1), it is worth to investigate this in detail. We therefore modeled Ni xxvii K α and Fe xxv K β lines individually. Fig. 6 shows the spectrum and the best-fit model. The modeled lines are listed in Table 6.

Strictly speaking, using fixed values of line centroids and widths is not correct because those quantities change with temperature. In addition, we approximated the line complex as a Gaussian whose line centroid and width calculated from the model may not be the same after being convolved with the instrument response. To properly compare our fit results with the theory, we simulated spectra and fit them the same way we fit the real data. Fig. 7 shows the observed line ratios and results from simulated VAPEC spectra with $9 \text{ Ni}_{\odot}/\text{Fe}_{\odot}$. 100 spectra were produced at each temperature and the flux was kept at the same level as that of the data. From the good match of fitted results from simulations to the direct model prediction, we confirmed that the fitting is accurate enough to measure the line flux, though only Fe xxv K α and Fe xxvi K α lines are precise enough for temperature determination. Table 7 shows the temperature and abundances, inferred from a single-temperature APEC model. The iron line temperature is in very good agreement with the continuum temperature for both *Chandra* and *XMM-Newton* data. All the *Chandra* and *XMM-Newton* observed line fluxes, except Fe xxv K β , are consistent with each other (after an overall 9% adjustment to the flux). Using Fe xxv+xxvi K α and Ni xxvii K α line flux, we obtain accordant Fe and Ni abundances from both instruments. The larger Fe and Ni abundances found in §3.1 for *Chandra* data are likely due to

TABLE 7
SUMMARY OF LINE ANALYSIS

		<i>Chandra</i>	<i>XMM</i> MOS
Continuum			
T	(keV)	$10.3^{+2.2}_{-0.8}$	$9.7^{+0.8}_{-1.1}$
Emission lines			
T^a	(keV)	$9.6^{+0.5}_{-0.5}$	$10.1^{+0.7}_{-0.7}$
Ni/Fe ^b †	($\text{Ni}_{\odot}/\text{Fe}_{\odot}$)	$8.4^{+3.7}_{-3.6}$	$1.4^{+1.8}_{-1.4}$
Ni/Fe ^c †	($\text{Ni}_{\odot}/\text{Fe}_{\odot}$)	$5.5^{+3.2}_{-3.1}$	$3.7^{+1.6}_{-2.1}$
Fe ^d †	(Z_{\odot})	0.31 ± 0.02	0.32 ± 0.03
Ni ^e †	(Z_{\odot})	$1.23^{+0.50}_{-0.91}$	$1.08^{+0.52}_{-0.65}$

^a from Fe xxvi K α /Fe xxv K α .

^b from (Ni xxvii K α +Fe xxv K β)/Fe xxvi K α .

^c from Ni xxvii K α /Fe xxvi K α .

^d from (Fe xxvi K α +xxv K α)/continuum.

^e from Ni xxvii K α /continuum.

† assuming $T = 10$ keV.

the higher temperature determined by the broad-band spectrum and the much stronger Fe xxv K β line.

As discussed previously, the 2T analysis of *Chandra* data suggested that another spectral component is needed if no absorption edge modeling is applied. Fig. 8 shows the line ratios predicted by the best-fit models from §3.2 over a wide range in temperature for the hot phase. Since the spectral energy range used in this fitting is far enough from the Si edge, it is not necessary to modify the spectral model even if the Si edge indeed needs to be corrected. The broad-band *Chandra* spectrum is not sensitive to the hot phase temperature of the 2T model once it exceeds 15 keV (Fig. 4). With the good constraint from the Fe xxvi K α /Fe xxv K α line ratio, models with $T_{\text{hot}} > 20$ keV, which are composed of great amounts of cooler gas, are rejected. Meanwhile, the ratio of higher energy states (Ni xxviii K α , Fe xxvi K β , Fe xxv K γ , K δ) to the well-measured Fe xxvi K α line suggests that models with lower T_{hot} are preferable.

As for the 2T models based on *Chandra* with an absorption edge model and *XMM-Newton* broad-band spectra, predicted line ratios all agree with the observed value. In fact, models with $T_{\text{hot}} > 20$ keV from *XMM-Newton* data are essentially a one temperature model, since the normalization of the hot component in these models is zero. Adding the fact that an additional temperature component does not significantly improve the χ^2 of the fit for those spectra and the remarkably good agreement on the temperature measured by the continuum and the iron lines from both *Chandra* and *XMM-Newton*, we conclude that the simple 1T model is adequate to describe the X-ray emission from the central 3' region of A1689.

4. DEPROJECTION ANALYSIS

Assuming that the hotter phase gas has the 3D temperature profile of L08, the radial distribution of the cooler gas can be derived. We extracted spectra from concentric annuli up to $8.8'$ ($1.2 h^{-1}\text{Mpc}$). The emission from each shell in three-dimensional space was modeled with an absorbed two-temperature APEC model with T_{hot} fixed at the value of L08 and then projected by the PROJECT model in XSPEC. Because of the complexity of this model, we used coarser annular bins than those used in

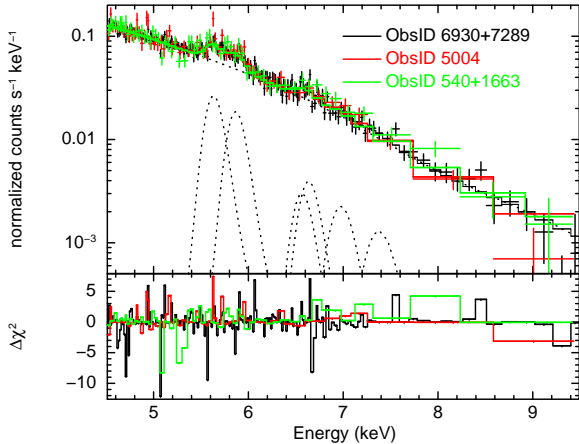


FIG. 6.— The 4.5-9.5 keV *Chandra* spectrum of the central 3' region. The spectrum is modeled with an absorbed thermal bremsstrahlung plus the seven Gaussian lines listed in Table 3.4.

L08. Data of L08 were binned using the weighting scheme of Mazzotta et al. (2004) to produce a spectroscopic-like temperature. T_{cool} , abundance, and the normalization of both components were free to vary. The outermost two annuli were background dominated, so spectra were binned to have at least 15 net counts per bin at $r = 4.8'-6.5'$ ($625-852 h^{-1}\text{kpc}$) and 2 net counts at $r = 6.5'-8.8'$ ($852-1161 h^{-1}\text{kpc}$) (see §2.5). L08 predicted the gas temperature only up to $721 h^{-1}\text{kpc}$, and that temperature was slightly below the observed one. Therefore, we allowed T_{hot} to change in the last two bins. The cold component was removed and the abundance was fixed at 0.2 solar in these regions in order to constrain the rest of the parameters better.

Assuming two phases in pressure equilibrium, the volume filling fraction of the i th component can be obtained from

$$f_i = \frac{\text{Norm}_i T_i^2}{\sum_j \text{Norm}_j T_j^2} \quad (1)$$

(e.g., Sanders & Fabian 2002). Once f_i is determined, the gas density $\rho_{gi} = \mu_e m_p n_{ei}$ can be derived from

$$\text{Norm}_i = \frac{10^{-14}}{4\pi((1+z)D_A)^2} \int n_{ei} n_{Hi} f_i dV, \quad (2)$$

where n_H/n_e and μ_e are calculated from a fully ionized plasma with the measured abundance (He abundance is primordial, and others are from Anders & Grevesse 1989). For $Z = 0.3 Z_{\odot}$, $n_H/n_e = 0.852$ and $\mu_e = 1.146$. Fig. 9 shows the results of this deprojected 2T analysis. The 1T modeling, in which emission from each shell has only one component, and the results from L08, are also shown. If the cluster has a temperature profile of L08, then 70-90% of the space within $250 h^{-1}\text{kpc}$ is occupied by the "cool" component with a temperature of ~ 10 keV, based on *Chandra* absorption edge corrected data, and this gas constitutes 90% of the total gas mass.

Kawahara et al. (2007) show that local density and temperature inhomogeneities do not correlate with each other in simulated clusters, which undermines the assumption of two phases in thermal pressure equilibrium. However, other cosmological simulations find that gas

TABLE 8
TOTAL MASS PROFILE

r ($h^{-1}\text{kpc}$)	$M_{1T+\text{edge}}$ ($10^{14}h^{-1}M_{\odot}$)	$M_{2T+\text{edge}}$ ($10^{14}h^{-1}M_{\odot}$)	M_{2T} ($10^{14}h^{-1}M_{\odot}$)
32^{+21}_{-13}	$0.06^{+0.01}_{-0.01}$	$0.09^{+0.09}_{-0.08}$	$0.08^{+0.01}_{-0.01}$
94^{+72}_{-41}	$0.44^{+0.01}_{-0.01}$	$0.67^{+0.13}_{-0.19}$	$0.63^{+0.02}_{-0.02}$
264^{+158}_{-99}	$1.96^{+0.04}_{-0.05}$	$2.67^{+0.60}_{-0.50}$	$3.03^{+0.06}_{-0.07}$
559^{+181}_{-137}	$4.01^{+0.80}_{-0.69}$	$5.23^{+1.67}_{-1.31}$	$5.57^{+0.53}_{-0.50}$
855^{+133}_{-115}	$7.50^{+6.04}_{-5.51}$	$7.33^{+4.84}_{-4.27}$	$7.00^{+3.88}_{-3.76}$

NOTE. — 2T assumption is only held within $625 h^{-1}\text{kpc}$. The upper and lower limits of r indicate the radii \bar{r} of two contiguous rings used to calculate the mass. See text for definitions of r and \bar{r} .

motions contribute about 5-20% of the total pressure support (e.g., Faltenbacher et al. 2005; Rasia et al. 2006; Lau et al. 2009). If the pressure balance is off by 20%, it will not significantly change the gas mass fraction ($\lesssim 4\%$) or the volume filling fraction ($\lesssim 8\%$).

5. MASS PROFILE

Given the 3D gas density and temperature profiles, the total cluster mass within a radius r can be estimated from the hydrostatic equilibrium equation (e.g., Sarazin 1988),

$$M(r) = -\frac{kT(r)r}{G\mu m_p} \left(\frac{d \ln \rho_g(r)}{d \ln r} + \frac{d \ln T(r)}{d \ln r} \right), \quad (3)$$

For $Z = 0.3 Z_{\odot}$, $\mu = 0.596$.

If the gas has two temperatures with two phases in pressure equilibrium, the total mass still can be derived from Eq. 3 with ρ_g , T replaced by $\rho_{g\text{hot}}$, T_{hot} , respectively.

5.1. Nonparametric method

To evaluate the derivatives in Eq. 3, we took the differences of deprojected temperature and the gas density in log space. The radius of each annulus was assigned at \bar{r} such that

$$F_{3D}(\bar{r}) \frac{4\pi}{3} (r_{\text{out}}^3 - r_{\text{in}}^3) = \int_{r_{\text{in}}}^{r_{\text{out}}} F_{3D}(r) 4\pi r^2 dr, \quad (4)$$

where F_{3D} is the deprojected flux density from a finely binned surface brightness profile, and r_{in} (r_{out}) is the inner (outer) radius of the annulus. The radius r outside of the brackets of Eq. 3 is taken at the geometric mean (i.e. the arithmetic mean in log scale) of the radii of two adjacent rings, $r = \sqrt{\bar{r}_i \bar{r}_{i+1}}$, and the temperature is linearly interpolated at this radius. Because errors from e.g. T and dT/dr are not independent, standard error propagation is not easily applied. Uncertainties are estimated from the distribution of 1000 Monte-Carlo simulations of T and ρ_g profiles. Fig. 9 shows the total mass profile from both 1T and 2T models and the results are listed in Table 8. Two-temperature modeling, based on the T_{hot} of L08, increases the total mass by 30-50% for all radii within $625 h^{-1}\text{kpc}$. Beyond that radius, the 2T assumption is not held because of the lack of constraint on T_{hot} .

Although the inclusion of an absorption edge in the spectral model greatly changes the derived composition

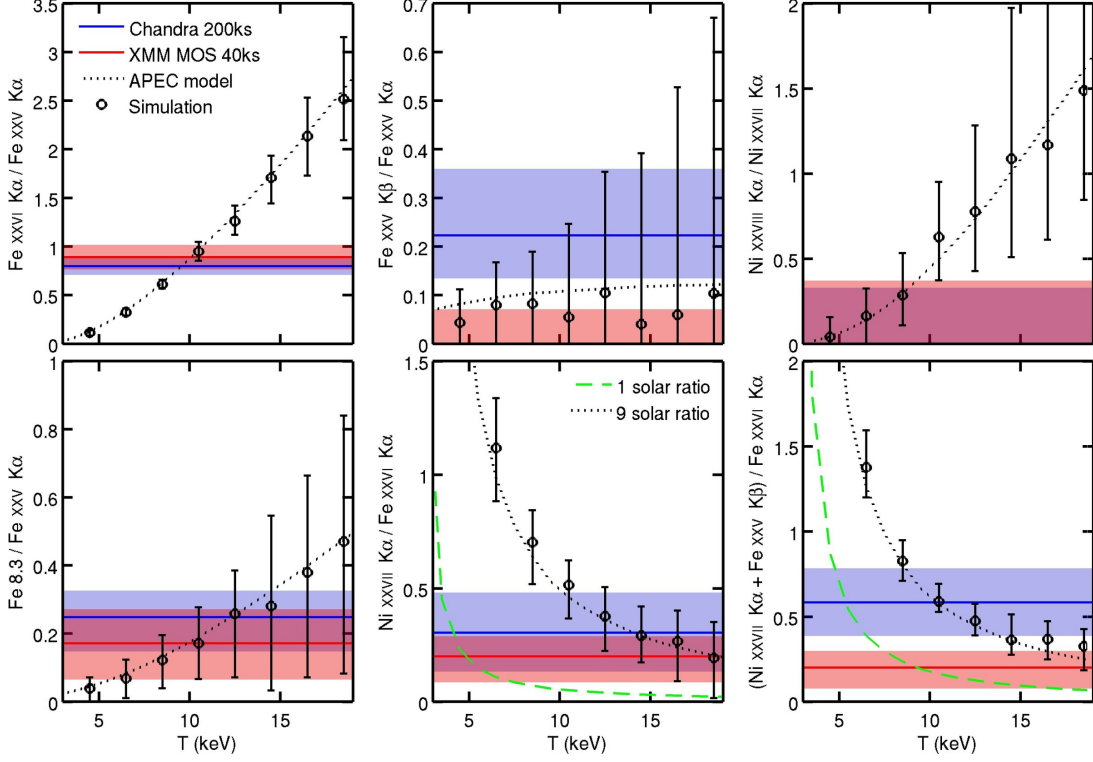


FIG. 7.— The predicted 1T plasma line ratio (dotted line) as a function of temperature, for various lines. The observed ratio and its 1σ confidence are shown as a solid line and shaded region. The circles show the fitted results of 100 simulated *Chandra* spectra drawn from a VAPEC model with $9 \text{ Ni}_{\odot}/\text{Fe}_{\odot}$.

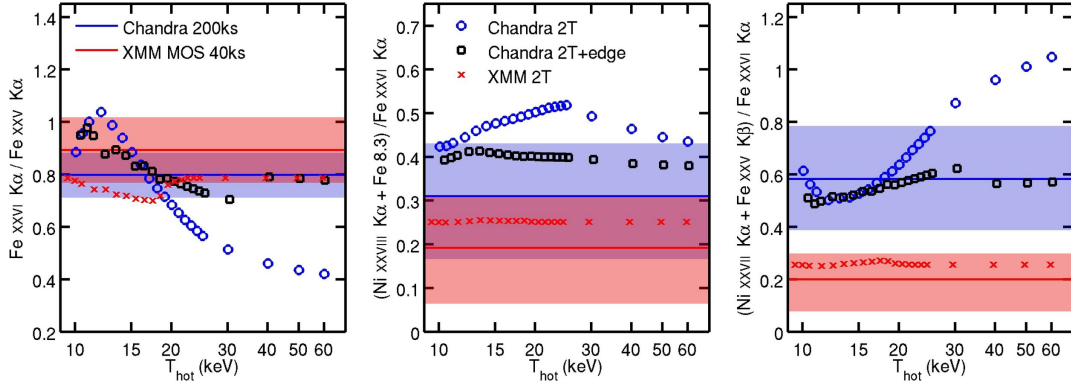


FIG. 8.— The predicted line ratio from the best-fit 2T (VAPEC) models (§3.2) as a function of the temperature of the hotter phase T_{hot} . The solid line and shaded region shows the observed ratio and its 1σ error. The x-axis is in log scale.

of the multi-phase plasma, it does not affect the mass measurement much. This is because we use a fixed T_{hot} profile. Once the temperature is determined, the total mass only depends on the logarithmic scale of the gas density, which produces $\sim 13\%$ difference at most.

5.2. 1T parametric method

If the temperature does not vary dramatically on small scales, we can obtain a mass profile with higher spatial resolution since the gas density can be measured in detail from the X-ray surface brightness with the assumption of a certain geometry of the cluster. To achieve this, modeling of the temperature and the gas density is necessary. Following the procedure of Vikhlinin et al. (2006), we project the 3D temperature and the gas den-

sity models along the line of sight and fit with the observed projected temperature and the surface brightness profiles. A weighting method by Mazzotta et al. (2004), Vikhlinin (2006) is used to predict a single-temperature fit to the projected multi-temperature emission from 3D space. This method has been shown (Nagai et al. 2007) to accurately reproduce density and temperature profiles of simulated clusters.

The gas density model is given by

$$n_p n_e = n_0^2 \frac{(r/r_c)^{-\alpha}}{(1 + r^2/r_c^2)^{3\beta - \alpha/2}} \frac{1}{(1 + r^\gamma/r_s^\gamma)^{\epsilon/\gamma}} + \frac{n_{02}^2}{(1 + r^2/r_{c2}^2)^{3\beta_2}}, \quad (5)$$

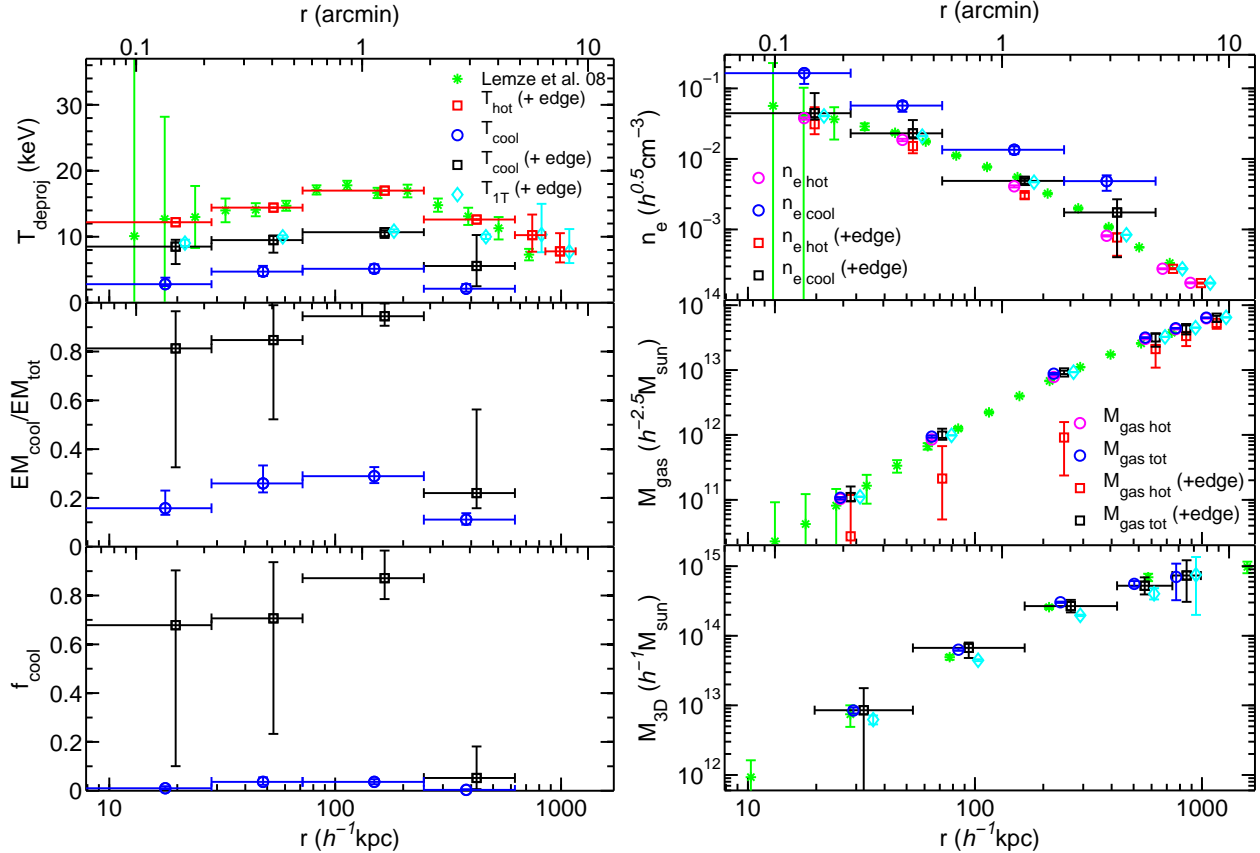


FIG. 9.— Temperature, emission measure ratio of the cool component $EM_{\text{cool}}/EM_{\text{tot}}$, volume filling fraction of the cool component f_{cool} , gas number density n_e , cumulative gas mass M_{gas} , and cumulative total mass M_{3D} profiles from the 2T deprojection analysis with an absorption edge correction (squares) and without the correction (circles). Also shown is the 1T analysis (diamonds) and results from Lemze et al. (2008a) (asterisks). T_{hot} of the first 4 annuli was fixed at the value derived from lensing and X-ray brightness data (Lemze et al. 2008a), which were grouped into fewer bins. The cool component of the last 2 bins was frozen at zero. The 2T assumption is held within $625 h^{-1}\text{kpc}$. X-data points of the 1T and 2T models have been shifted by +10% and -10% for clarity, and their error bars are also omitted.

which originates from a β model (Cavaliere & Fusco-Femiano 1978) modified by a power-law cusp and a steepening at large radii (Vikhlinin et al. 1999). The second term describes a possible component in the center, especially for clusters with small core radius. The temperature model is given by

$$T_{3D}(r) = T_0 \frac{(r/r_{\text{cool}})^{a_{\text{cool}}} + T_{\text{min}}/T_0}{1 + (r/r_{\text{cool}})^{a_{\text{cool}}}} \frac{(r/r_t)^{-a}}{(1 + (r/r_t)^b)^{c/b}}, \quad (6)$$

which is a broken power law with central cooling (Allen et al. 2001). Best-fit parameters for the gas density and temperature profiles are listed in Tables 9 and 10, respectively. Errors are estimated from the distribution of the fitted parameters of 1000 simulated projected temperature and surface brightness profiles generated according to the observed data and their measurement uncertainties. Since parameters are highly degenerate, some of the best-fit values are not covered by the upper or lower limits with the quoted confidence level (upper/lower bounds are for one parameter). The observed temperature and surface brightness profiles, the best-fit model, and the surface brightness residual are shown in Fig. 10. The model describes the data very well ($\chi^2/\text{dof}=154.3/155$). The best-fit T_{3D} and n_e models are shown in Fig. 11. Also

plotted are the profiles from the spectral deprojection fitting (§5.1). Compared to this nonparametric result, modeling T_{3D} and n_e can avoid fluctuations from the direct spectral deprojection, which is a common problem as the deprojection tends to amplify the noise in the data (see Appendix in Sanders & Fabian 2007).

Although the second break of the first term in Eq. 5 was designed to describe the steepening at $r_s > 0.3 r_{200}$ (Vikhlinin et al. 1999, 2006; Neumann 2005), we found that if the initial guess for r_s is not big enough, r_s tends to converge to a relatively small value, $\approx 200 h^{-1}\text{kpc}$, compared to the typical value of $400\text{--}3000 h^{-1}\text{kpc}$ for nearby relaxed clusters (Vikhlinin et al. 2006). It is possible to use the first core radius r_c or the core radius of the second component r_{c2} to account for the sharpening at $200 h^{-1}\text{kpc}$. This consequently yields a more reasonable r_s at $\approx 1 h^{-1}\text{Mpc}$. Both cases, small (Model 1) and large (Model 2) r_s , give acceptable fits with χ^2/dof of $153.4/155$ and $154.3/155$, respectively. However, large r_s is harder to constrain. This makes the mass estimate more uncertain at large radii than the small r_s case.

Comparing the surface brightness profile of the northeastern (NE) part to the southwestern (SW), Riemer-Sørensen et al. (2009) found that the NE part is 5-15% brighter outside $350 h^{-1}\text{kpc}$ and 25% under-luminous at

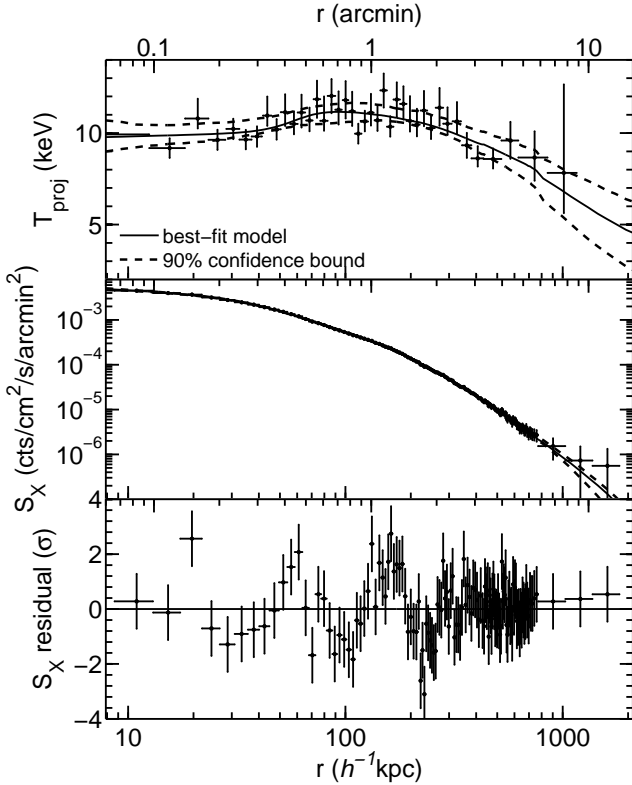


FIG. 10.— Projected temperature and surface brightness profiles with the best-fit model (solid lines) and its 90% confidence bounds (dashed lines). Bottom panel: residual between the surface brightness and the model. This fit gives a χ^2/dof of 154.3/155.

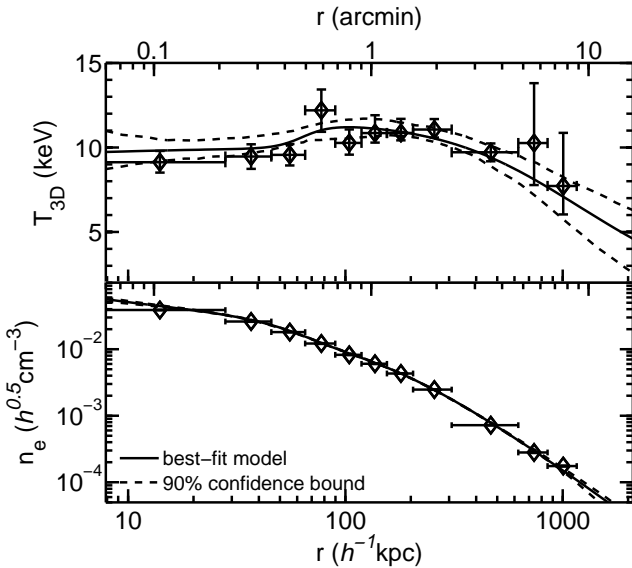


FIG. 11.— Best-fit T_{3D} and n_e models (solid lines) and 90% confidence bounds (dashed lines). Also shown are unparameterized results (diamonds) from §5.1.

$70 h^{-1}\text{kpc}$ than the SW. To see if this asymmetry can affect the mass estimate, we fit a symmetric model to the image and iteratively removed any part of the cluster that deviates significantly from the azimuthal mean, mainly the northern clump at $460 h^{-1}\text{kpc}$, the southern less luminous region at $330 h^{-1}\text{kpc}$, and possibly some point sources not completely removed beforehand. We did not exclude these regions from our temperature measurement since they were unlikely to bias the average temperature much for such a hot cluster, as shown in Fig. 4 that at least 10-20% of the total emission measure from another spectral component was needed in order to change the spectroscopic temperature by 1 keV. Best-fit gas density and temperature for these models are listed in Tables 9 and 10, labelled with Model 3 (small r_s) and 4 (large r_s).

The total mass profiles from these analytic gas density and temperature models are given in Table 11. We list the total mass at the radii where masses from the non-parametric method are evaluated (Table 8). The last entry of Table 11 shows the total mass at the boundary of the ACIS-I chips, $12'$ ($1.6 h^{-1}\text{Mpc} \approx r_{200}$), where S_X is detected at $\lesssim 1\sigma$. Removing asymmetric parts from the image or restricting r_s to be greater than $350 h^{-1}\text{kpc}$ increases the total mass estimate with $\lesssim 10\%$. Nonetheless, these differences are not significant. We combine samples of the best-fit parameters of substructures removed cases (Model 3 and 4) as our best result.

Fig. 12 shows a comparison of parametric and non-parametric mass profiles. The non-parametric mass profile is from a more finely binned deprojected data than those shown in Fig. 9. Results from these two methods are fully consistent with each other, although their errors are quite different. For the non-parametric method, we simply assign the observable, e.g. dT/dr , at a certain radius, so the uncertainty associated with the position is not included in the error on the mass, σ_M , but separately shown on the radius. Therefore, σ_M appears smaller if data are binned more coarsely. For the parametric method, the dependency of σ_M on the data binning is weaker. The departure from the model for any data point is assumed to be random noise and is filtered out through the fitting. Hence, σ_M reflects only the uncertainty of the fitted function and it depends strongly on the modeling.

5.3. Comparison with other studies

The total mass profiles of A04, based on *XMM-Newton*, and L08, a joint X-ray, strong and weak lensing study are also shown in Fig. 12. Our result is in good agreement with A04, but disagrees with L08 around $\sim 200 h^{-1}\text{kpc}$. To compare our mass estimate with other lensing works, we derived the total mass density and integrated it along the line-of-sight. The total mass density, ρ , is obtained through the hydrostatic equation,

$$4\pi G\rho = -\frac{k}{\mu_g m_p} (\nabla^2 T + T \nabla^2 \ln \rho_g + \nabla \ln \rho_g \cdot \nabla T). \quad (7)$$

For the nonparametric method, we evaluated Eq. 7 in a similar fashion as we did in §5.1. Errors were estimated from the Monte-Carlo simulations of deprojected T and ρ_g profiles. Fig. 13 shows the surface mass density profiles from both parametric and nonparametric meth-

TABLE 9
BEST-FIT PARAMETERS FOR THE GAS DENSITY (Eq.5)

	n_0 $10^{-2}h^{1/2}\text{cm}^{-3}$	r_c 10^2h^{-1}kpc	r_s 10^2h^{-1}kpc	α	β	ϵ	n_{02} $10^{-1}h^{1/2}\text{cm}^{-3}$	r_{c2} 10^2h^{-1}kpc	β_2	γ
(1)	$3.68^{+0.01}_{-0.78}$	$0.25^{+0.10}_{-0.00}$	$1.99^{+0.19}_{-0.10}$	$0.37^{+0.32}_{-0.13}$	$0.36^{+0.04}_{-0.03}$	$1.89^{+0.24}_{-0.28}$	$0.20^{+0.03}_{-0.03}$	$2.04^{+0.26}_{-0.49}$	$7.10^{+2.54}_{-2.63}$	$4.64^{+1.23}_{-0.99}$
(2)	$0.78^{+0.14}_{-0.07}$	$1.65^{+0.11}_{-0.21}$	$11.5^{+17.4}_{-0.1}$	$1.14^{+0.08}_{-0.16}$	$0.73^{+0.02}_{-0.04}$	$0.50^{+3.66}_{-0.48}$	$0.27^{+0.03}_{-0.01}$	$1.72^{+0.16}_{-0.72}$	$6.10^{+0.85}_{-3.65}$	$2.56^{+7.06}_{-0.28}$
(3)	$2.46^{+1.08}_{-0.22}$	$0.46^{+0.03}_{-0.15}$	$2.70^{+0.19}_{-0.15}$	$0.73^{+0.09}_{-0.39}$	$0.44^{+0.02}_{-0.05}$	$1.91^{+0.36}_{-0.09}$	$0.19^{+0.02}_{-0.04}$	$2.33^{+0.14}_{-0.89}$	$10.0^{+0.0}_{-6.1}$ ^a	$7.52^{+0.46}_{-2.56}$
(4)	$0.64^{+0.33}_{-0.19}$	$1.98^{+0.80}_{-0.60}$	$10.2^{+27.9}_{-6.72}$	$1.20^{+0.11}_{-0.56}$	$0.77^{+0.02}_{-0.12}$	$1.45^{+2.91}_{-1.33}$	$0.27^{+0.09}_{-0.02}$	$1.77^{+0.19}_{-1.22}$	$6.01^{+0.69}_{-5.08}$	$2.08^{+8.52}_{-0.71}$

NOTE. — (1) small r_s , (2) large r_s , (3) small r_s with northern clumps removed, (4) large r_s with northern clumps removed. Errors are 95% CL for one parameter from 1000 Monte-Carlo simulations. Since parameters are highly degenerate, some of the best-fit values are not covered by the upper and lower limits at this confidence level.

^a parameters hit the hard limit.

TABLE 10
BEST-FIT PARAMETERS FOR THE TEMPERATURE (Eq.6)

	T_0 keV	T_{\min}/T_0	r_{cool} 10^2h^{-1}kpc	r_t 10^2h^{-1}kpc	a	b	c	d
(1)	$12.7^{+6.9}_{-2.8}$	$0.73^{+0.25}_{-0.34}$	$0.67^{+1.66}_{-0.29}$	$12.5^{+20.8}_{-6.8}$	$0.02^{+0.11}_{-0.14}$	$0.86^{+0.64}_{-0.36}$	$0.81^{+1.82}_{-0.40}$	$2.96^{+2.14}_{-2.45}$
(2)	$12.1^{+7.2}_{-3.4}$	$0.87^{+0.11}_{-0.41}$	$0.64^{+1.75}_{-0.15}$	$8.36^{+21.7}_{-0.93}$	$-0.02^{+0.16}_{-0.11}$	$1.37^{+0.65}_{-0.80}$	$0.89^{+2.11}_{-0.43}$	$6.78^{+0.83}_{-6.30}$
(3)	$14.4^{+5.8}_{-5.3}$	$0.40^{+0.60}_{-0.13}$	$0.77^{+1.42}_{-0.28}$	$28.6^{+0.5}_{-25.0}$	$0.11^{+0.10}_{-0.24}$	$0.40^{+1.11}_{-0.03}$	$0.59^{+1.56}_{-0.19}$	$1.44^{+3.86}_{-1.17}$
(4)	$11.8^{+8.4}_{-2.9}$	$0.86^{+0.14}_{-0.50}$	$0.74^{+1.84}_{-0.29}$	$9.08^{+23.1}_{-2.42}$	$-0.01^{+0.17}_{-0.12}$	$1.68^{+0.81}_{-1.15}$	$1.32^{+1.64}_{-0.92}$	$7.07^{+6.57}_{-6.57}$

NOTE. — (1) small r_s , (2) large r_s , (3) small r_s with northern clumps removed, (4) large r_s with northern clumps removed. Errors are 95% CL for one parameter from 1000 Monte-Carlo simulations.

TABLE 11
PARAMETRIC TOTAL MASS PROFILE

r ($h^{-1}\text{kpc}$)	$M(r)$ ($10^{14}h^{-1}M_{\odot}$)			
	(1)	(2)	(3)	(4)
32	$0.07^{+0.01}_{-0.01}$	$0.07^{+0.01}_{-0.01}$	$0.07^{+0.01}_{-0.01}$	$0.07^{+0.01}_{-0.01}$
94	$0.46^{+0.01}_{-0.02}$	$0.46^{+0.01}_{-0.03}$	$0.47^{+0.02}_{-0.02}$	$0.44^{+0.03}_{-0.02}$
264	$2.01^{+0.07}_{-0.03}$	$1.92^{+0.09}_{-0.02}$	$1.92^{+0.09}_{-0.03}$	$1.94^{+0.08}_{-0.08}$
559	$4.15^{+0.32}_{-0.02}$	$4.43^{+0.18}_{-0.11}$	$4.64^{+0.27}_{-0.03}$	$4.86^{+0.15}_{-0.51}$
855	$5.73^{+0.46}_{-0.05}$	$6.37^{+0.35}_{-0.36}$	$6.41^{+0.40}_{-0.23}$	$7.03^{+0.71}_{-1.00}$
1579	$8.60^{+0.99}_{-1.02}$	$9.52^{+2.32}_{-0.97}$	$9.85^{+0.53}_{-1.52}$	$9.55^{+3.31}_{-1.43}$

NOTE. — (1) small r_s , (2) large r_s , (3) small r_s with northern clumps removed, (4) large r_s with northern clumps removed. Errors are 68% CL from 1000 Monte-Carlo simulations.

ods, along with the HST/ACS strong lensing analysis of Broadhurst et al. (2005a), and the combined Subaru distortion and depletion data by Umetsu & Broadhurst (2008). Since it requires at least 3 points to calculate the second derivative, ρ at the boundary is unknown. This will introduce additional systematic errors to the inner and the outer projected profile. To demonstrate how this may affect our nonparametric result, we insert two artificial points at $1''$ ($2 h^{-1}\text{kpc}$) and $13'$ ($1.7 h^{-1}\text{Mpc}$) to the nonparametric T and ρ_g profiles with their values estimated from the parametric model. The projected density derived this way is shown in red filled diamonds in Fig. 13. The X-ray data are consistent with those from the weak lensing, but disagree with the strong lensing analysis. Although the nonparametric data appears to agree with the strong lensing estimate at $r = 80 h^{-1}\text{kpc}$, this is probably due to the temperature fluctuation mentioned in §5.2.

The mass discrepancy is manifested when comparing

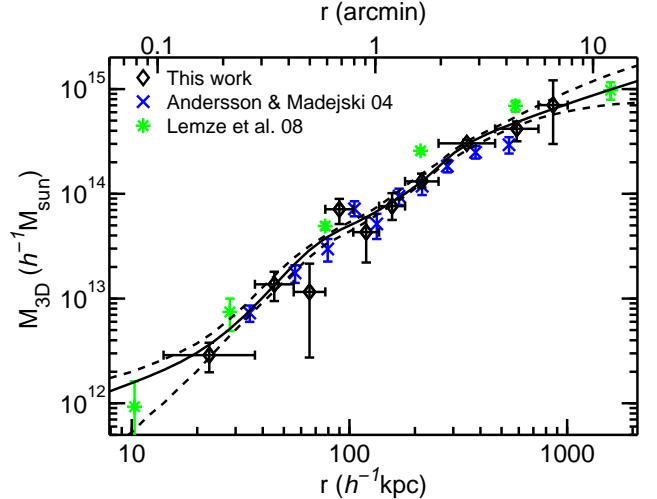


FIG. 12.— The parametric mass profile (solid line) compared to the unparameterized result (diamonds). Dashed lines show the 95% confidence bounds. Also shown are *XMM-Newton* result from A04 (crosses) and combined X-ray, strong and weak lensing analysis of L08 (asterisks). The mass profile of L08 is mainly determined by the lensing data.

the cumulative projected mass profiles, M_{2D} , shown in Fig. 14. The weak lensing M_{2D} profile of Umetsu & Broadhurst (2008) includes the integration of the data of Broadhurst et al. (2005a) in the inner region. Uncertainties are from Monte-Carlo simulations of the convergence profiles. The last 3 data points of Umetsu & Broadhurst (2008) ($1-2.3 h^{-1}\text{Mpc}$) are discarded since only the upper limits are available. Also shown are parametric strong lensing profiles (Halkola et al. 2006; Limousin et al. 2007), and other X-ray analyses (A04;

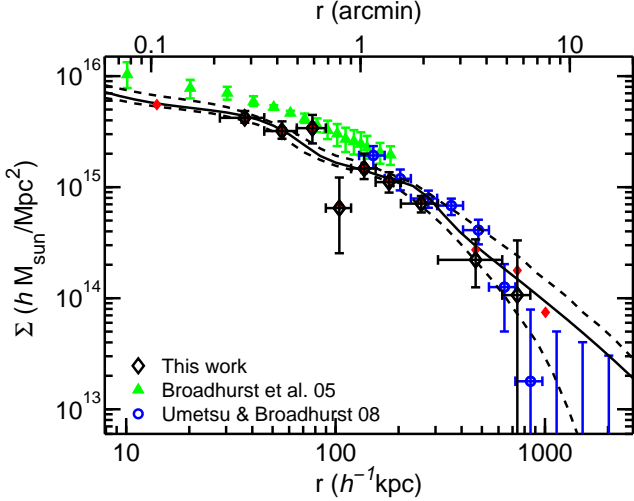


FIG. 13.— Surface mass density profiles from non-parametric (open diamonds) and parametric X-ray model (solid and dashed lines, 95% CL), compared to HST/ACS strong lensing analysis of Broadhurst et al. (2005a) (triangles), and combined Subaru distortion and depletion data by Umetsu & Broadhurst (2008), based on a maximum entropy method (circles). Filled diamonds show the mass from the nonparametric T_{3D} and n_e profiles that include estimations from the parametric result at $1''$ ($2 h^{-1}\text{kpc}$) and $13'$ ($1.7 h^{-1}\text{Mpc}$).

Riemer-Sørensen et al. 2009). To convert M_{3D} to M_{2D} , A04 assume that the last data point reached the cluster mass limit, which unavoidably leads to underestimations especially at large radii. Riemer-Sørensen et al. (2009) use only the SE part of the cluster and four of the *Chandra* observations (excluding ObsID 540) and derive M_{2D} based on a best-fit NFW model fit to the M_{3D} profile. Their mass profile is generally lower than our estimate at most radii. This is contradictory to most findings that claim that the hydrostatic mass is underestimated in unrelaxed systems (e.g., Jeltama et al. 2008). Using such reasoning, and removing the NE part, presumably disturbed according to Riemer-Sørensen et al. (2009), should increase the overall mass estimate. The X-ray M_{2D} is 25-40% lower than that of lensing within 200 $h^{-1}\text{kpc}$, corresponding to a $\sim 1.4 \times 10^{14} h^{-1}M_{\odot}$ difference in the total projected mass.

5.4. NFW profile parameters

The total mass profile M_{3D} was fit to the NFW model (Navarro et al. 1997) to obtain the mass and the concentration parameter. To fit the nonparametric data, we weighted each point according to its vertical and horizontal errors, given by,

$$\sigma^2 = \sigma_M^2 + \sigma_r^2 \left(\frac{dM}{dr} \right)^2, \quad (8)$$

where σ_r is assigned to be 68% of the width of the horizontal error bar and dM/dr is iteratively evaluated from the NFW model until it converges. In the parametric approach, a NFW model was fit to the parametrized mass profile that evaluated only at the radii where the projected temperature was measured with errors estimated from the standard deviation of a sample of mass profiles constructed from the simulated T_{proj} and S_X profiles described in §5.2. We repeated this procedure for all of the

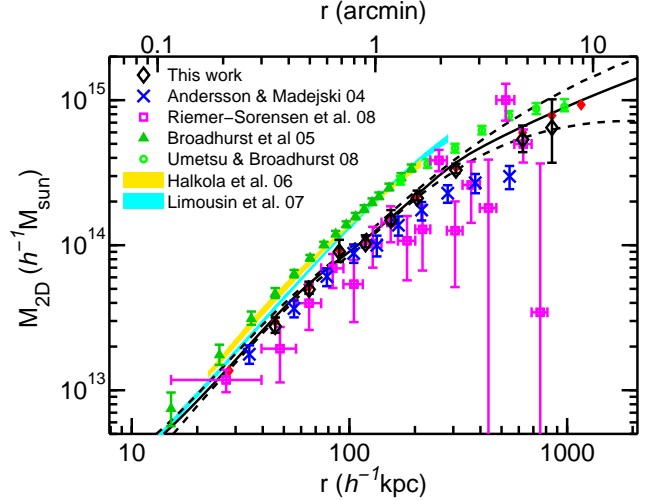


FIG. 14.— Projected mass profiles from non-parametric (open diamonds) and parametric analyses (solid and dashed lines, 95% CL), compared to *XMM-Newton* result from A04 (crosses), *Chandra* result by Riemer-Sørensen et al. (2009) (squares), HST/ACS and Subaru results by Broadhurst et al. (2005a) (triangles) and Umetsu & Broadhurst (2008) (circles). We integrated the lensing surface mass profile (shown in Fig. 13) and estimated its uncertainties from Monte-Carlo simulations. Also shown are parametric strong lensing profiles of Halkola et al. (2006) and Limousin et al. (2007) (shaded regions, 68% CL). Riemer-Sørensen et al. (2009) used only SW part of the X-ray data and converted M_{3D} to M_{2D} with a NFW profile. A04 assumed that the last data point reached the cluster mass limit. Filled diamonds, same as Fig. 13.

mass profiles in the sample. Resulting NFW parameters were used to estimate the uncertainty.

Table 12 lists the best-fit NFW parameters, M_{200} and c_{200} , for the total mass from both methods and from other studies, all converted to the adopted cosmology. Compared to other X-ray studies, our derived M_{200} is 30-50% higher, closer to weak lensing results. The differences between our NFW parameters and those of A04 from *XMM-Newton* are primarily attributed to their slightly lower but yet consistent mass at the last data point (Fig. 12). This demonstrates that the accurate mass measurement at large radii, where systematic errors are usually the greatest, is crucial to the determination of NFW parameters.

Our results are consistent with weak lensing measurements, but with a lower concentration than what recent weak lensing studies seem to suggest (Umetsu & Broadhurst 2008; Corless et al. 2009). When these analyses are added with strong lensing information, a very tight constraint on the concentration parameter can be obtained, giving $C_{200} = 9.9^{+0.8}_{-0.7}$ (Umetsu & Broadhurst 2008), which hardly can be reconciled with our value, $5.3^{+1.3}_{-1.2}$. However, if the gas emission is modeled with two spectral components with T_{hot} from L08, the X-ray derived concentration is in a closer agreement to those of combined strong and weak lensing studies, but this also implies that the majority of the gas is in the cool phase and occupies most of the intracluster space (§3.2).

5.5. Gas mass fraction

The cumulative gas fraction $f_{\text{gas}} = M_{\text{gas}}/M_{\text{total}}$, derived from our best-fit T_{3D} and n_e model, is $0.098^{+0.003}_{-0.004}$

TABLE 12
COMPARISON OF BEST-FIT NFW PARAMETERS

Method	Instrument	M_{200} ($10^{15}h^{-1}M_{\odot}$)	c_{200}	χ^2/dof	Reference
Spherical model					
X-ray (1T+edge)	Chandra	$1.16^{+0.45}_{-0.27}$	$5.3^{+1.3}_{-1.2}$	6.3/8	this work
X-ray (parametrized T_{3D} , n_e)	Chandra	$0.94^{+0.11}_{-0.06}$	$6.6^{+0.4}_{-0.4}$		this work
X-ray (2T ^a)	Chandra	$1.45^{+0.36}_{-0.25}$	$7.6^{+1.3}_{-1.2}$	2.2/3	this work
X-ray (2T ^a +edge)	Chandra	$1.12^{+0.53}_{-0.29}$	$9.3^{+0.7}_{-2.8}$	0.1/3	this work
X-ray (1T)	XMM-Newton	0.63 ± 0.36	$7.6^{+1.7}_{-2.6}$	7.6/8	A04
X-ray (1T)	Chandra	0.55	10.1^d	1.6/13	Riemer-Sørensen et al. (2009)
SL	ACS	2.29	$6.3^{+1.8}_{-1.6}$		Broadhurst et al. (2005a)
SL	ACS	2.16 ± 0.32	5.8 ± 0.5	0.8/11	Halkola et al. (2006)
WL	CFHT	0.97 ± 0.13	7.4 ± 1.6		Limousin et al. (2007)
WL	CFHT	0.90 ± 0.17	13.1 ± 7.5		Corless et al. (2009)
WL	Subaru	1.24 ± 0.14	$10.5^{+4.4}_{-2.6}$	332/834	Umetsu & Broadhurst (2008)
SL+WL	ACS+Subaru	1.22 ± 0.13	$10.8^{+1.1}_{-0.9}$	13.3/20	Broadhurst et al. (2005b)
SL+WL	ACS+Subaru	1.31 ± 0.11	$9.9^{+0.8}_{-0.7}$	335/846	Umetsu & Broadhurst (2008)
SL+WL+X-ray (S_X)	ACS+Subaru+Chandra	1.42	$9.7^{+0.8}_{-0.7}$	15.3/24	L08
Triaxial model					
SL+WL ^b	ACS+Subaru	$1.15^{+0.26}_{-0.45}$	$13.4^{+1.8}_{-10.2}$	378/362	Oguri et al. (2005)
WL ^c	CFHT	0.83 ± 0.16	12.0 ± 6.6		Corless et al. (2009)

NOTE. — see Comerford & Natarajan (2007); Umetsu & Broadhurst (2008); Corless et al. (2009) for a more complete compilation.

^a with T_{hot} from L08

^b under a flat prior on the axis ratios.

^c under a prior on the halo orientation that favors the line-of-sight direction.

^d converted from best-fit parameters, $\rho_0 = 7.79 \times 10^6 M_{\odot} \text{kpc}^{-3}$, $r_s = 174 \text{ kpc}$ ($h = 0.7$, $\Omega_m = 0.28$, and $\Omega_{\lambda} = 0.72$), of Riemer-Sørensen et al. (2009), not consistent with their quoted value of 5.6 since they did not adopt the commonly defined c_{200} , the concentration at r_{200} where the enclosed mean density is 200 times the critical density (private communication).

$h_{70}^{-1.5}$ at r_{2500} ($493^{+11}_{-10} h^{-1} \text{kpc}$), $\sim 20\%$ higher than what is found using *XMM-Newton* data (A04). In spite of this seemingly large difference, the data agree that f_{gas} does not converge at r_{2500} . Much like in the case of A1689, the low- z relaxed cluster A1413 does not have a strong cooling core and also has a steadily rising f_{gas} profile out to r_{500} (Pratt & Arnaud 2002). Comparing the f_{gas} profile of A1413 with another nearby prominent cooling core cluster, A478, Pointecouteau et al. (2004) speculate that the flatter f_{gas} profile of A478 is related to the presence of a cooling core. Our f_{2500} is 11% lower than the mean gas fraction of Allen et al. (2008) derived from 42 relaxed clusters observed with *Chandra*, but our f_{500} , $0.12 \pm 0.01 h_{70}^{-1.5}$, agrees within 1% of the $M - f_{\text{gas}}$ relation of Vikhlinin et al. (2009).

6. DISCUSSION

Nagai et al. (2007) show that following the data analysis of Vikhlinin et al. (2006), the hydrostatic mass is underestimated by $14 \pm 6\%$ within estimated r_{2500} for simulated clusters visually classified as "relaxed". Based on the X-ray morphology, A1689 is likely to be categorized as a relaxed cluster. The X-ray centroid is within $3''$ of the lensing and optical centers (Andersson & Madejski 2004), with a very minimal centroid shift or asymmetry (Hashimoto et al. 2007). At the X-ray estimated r_{2500} of $493 h^{-1} \text{kpc}$, we derive an enclosed hydrostatic mass of $(4.2 \pm 0.3) \times 10^{14} h^{-1} M_{\odot}$, $\approx 30\%$ lower than the lensing mass from L08. At $r = 200 h^{-1} \text{kpc}$, this becomes a 50% difference (see Fig. 12). Such a strong bias is not seen in the relaxed cluster sample of Nagai et al. (2007), assuming that the lensing mass is unbiased, although this is not

TABLE 13
COMPARISON OF M_{500}

Method	M_{500} ($10^{14} h^{-1} M_{\odot}$)	r_{500} ($h^{-1} \text{Mpc}$)
parametrized T_{3D} , n_e	$7.3^{+1.3}_{-0.5}$	$1.01^{+0.06}_{-0.03}$
$M_{500} - T_X$ [†]	7.7 ± 0.2	1.03 ± 0.01
$M_{500} - Y_X$ ^{† a}	$7.7^{+0.5}_{-1.2}$	$1.03^{+0.02}_{-0.06}$

[†] Scaling relations from Vikhlinin et al. (2009) with indices fixed to self-similar theory values. Errors only reflect the measurement uncertainties. Dispersions of the relation is not included. $T_X = 10.1 \pm 0.2 \text{ keV}$, measured from $r = 1.14' - 7.6'$ ($\approx 0.15r_{500} - r_{500}$).

^a By solving Eq. 14 of Vikhlinin et al. (2009). The final $Y_X = T_X \times M_{\text{gas}}$ determined at r_{500} is $(5.1^{+0.5}_{-1.2}) \times 10^{14} h^{-2.5} M_{\odot} \text{ keV}$.

unusual for "unrelaxed" clusters, referring to those with secondary maxima, filamentary structures, or significant isophotal centroid shifts.

Table 13 shows the comparison of measured M_{500} with others derived from the $M_{500} - Y_X$ and $M_{500} - T_X$ relations of Vikhlinin et al. (2009), calibrated from 49 low- z and 37 high- z with $\langle z \rangle = 0.5$ clusters observed with *Chandra* and *ROSAT*. A very good agreement has been achieved between these estimates. Since the $M_{500} - Y_X$ relation is insensitive to whether the cluster is relaxed or not (Kravtsov et al. 2006) and merging clusters tend to be cool for their mass (Mathiesen & Evrard 2001), consistency among these mass estimates indicates that A1689 is relaxed in the sense that it behaves like other "relaxed" clusters on the scaling relation.

On the other hand, projection effects, such as triaxial halos or chance alignments, always have to be taken into account when comparing projected (lensing) and three-dimensional (X-ray) mass estimates. From kinematics of about 200 galaxies in A1689, Lokas et al. (2006) suggest that there could be a few distant, possibly non-interacting, substructures superposed along the line of sight. Lemze et al. (2008b), based on a $0.5 \times 0.5 \text{ deg}^2$ VLT/VIMOS spectroscopic survey from Czoske (2004) which includes ~ 500 cluster members, disagree with this projection view. They conclude that only one identifiable substructure at $+3000 \text{ km/s}$, $1.5'$ to the NE (The X-ray clump is at $\sim 3.5'$ NE). This background group is seen in the strong lensing mass analysis (Broadhurst et al. 2005a), but is determined not to be massive ($< 10\%$ of the total mass in the strong lensing region). Nonetheless, the higher than usual velocity dispersion in the cluster center, $\sim 2100 \text{ km/s}$, indicates that the central part is quite complex (Czoske 2004). This may also imply that the halo is elongated in the line-of-sight direction, as galaxies move faster along the major axis.

For powerful strong lens systems, like A1689, halo sphericity is never a justified assumption (e.g., Hennawi et al. 2007). Oguri & Blandford (2009) show that these "superlens" clusters almost always have their major axes aligned along the line-of-sight, with more circular appearances in projection and $\sim 40 - 60\%$ larger concentrations than other clusters with similar masses and redshifts. Gavazzi (2005) demonstrates that using a prolate halo with axis ratio ~ 0.4 , they were able to explain the mass discrepancy between the lensing and X-ray estimates of cluster MS2137-23. This cluster has a well defined cool core (e.g., Andersson et al. 2009), thus presumably relaxed, and yet a factor of 2 difference in the mass is not lessened with a multiphase model for the core region (Arabadjis et al. 2004). In contrast, triaxial modeling not only solves the mass inconsistency, but also the high concentration problem and the misalignment between stellar and dark matter components in MS2137-23 (Gavazzi 2005).

To see how the triaxiality changes our mass measurements, we modeled T_{3D} and ρ_g with prolate profiles, by replacing r in Eq. 5 and 6 with $(x^2/a^2 + y^2/b^2 + z^2/c^2)^{1/2}$, where we assumed $a = b < c$ and the major axis, z -axis, is perfectly aligned along the line-of-sight. Following the same analysis outlined in §5.2 but with different projection factors, we obtained best-fit T_{3D} and ρ_g profiles. The derived mass profiles under various axis ratios a/c are shown in Fig. 15. The uncertainties on $\Sigma(r)$ and $M_{2D}(r)$ are similar to those in Figs. 13 and 14. We integrated the density from $z = -4.5h^{-1}\text{Mpc}$ to $+4.5h^{-1}\text{Mpc}$ ($\approx 3r_{200}$ for $a/c=1$) for all the cases. The uncertainties of T_{3D} and ρ_g profiles at large radii ($\gtrsim 10\%$ at $r = r_{500}$ and increasing further afterward) does not significantly change the projected mass at smaller radii ($\lesssim 3\%$ within $500h^{-1}\text{kpc}$).

The total mass enclosed within a sphere of radius r , $M_{3D}(r)$, and the spherically averaged mass density, $\rho(r)$, are basically unchanged under different assumptions of triaxiality, considering the typical measurement uncertainty. The same conclusion was drawn by Piffaretti et al. (2003) and Gavazzi (2005), though they assumed a β or a NFW model with gas isothermality. For the

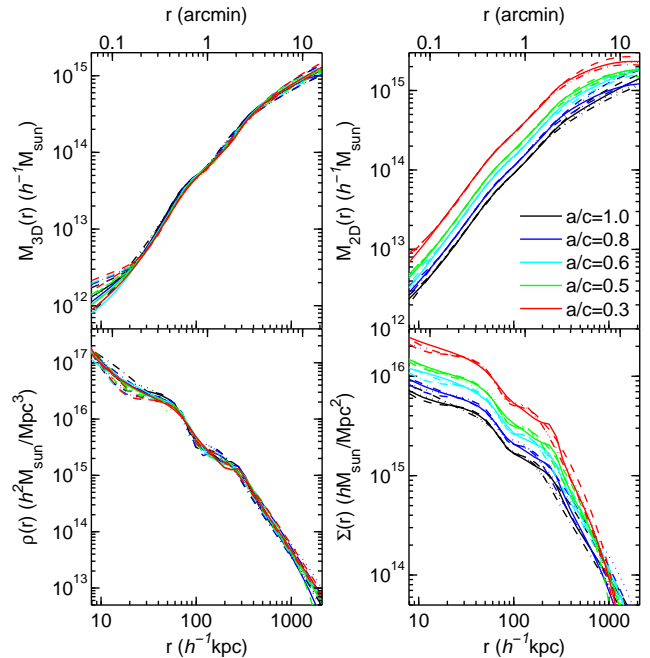


FIG. 15.— Best-fit mass profiles for various axis ratios a/c from Model 1 (dash-dot line), 2 (dotted line), 3 (solid line), and 4 (dashed line). *Top left*: total mass enclosed within a sphere of radius r , $M_{3D}(r)$. *Top right*: spherically average mass density $\rho(r)$. *Bottom left*: azimuthally average surface mass density $\Sigma(r)$. *Bottom right*: projected mass within a cylinder of radius r , $M_{2D}(r)$.

azimuthally averaged surface mass density $\Sigma(r)$ or the projected mass within a cylinder of radius r , $M_{2D}(r)$, a factor of 2 or more difference can be easily made by increasing the ellipticity. An axis ratio of 0.6, giving $M_{2D}(< 45'') = 1.4 \times 10^{14} h^{-1} M_{\odot}$ (by a factor of 1.6 increase), can resolve the central mass discrepancy, but overpredicts the mass by $\sim 40\%$ at large radii. For a ratio of 0.7, the X-ray mass estimate data agrees with those of strong and weak lensing within 1% ($-\sigma$) and 25% ($+\sigma$), respectively. Since the gas distribution is rounder than that of the DM, a larger axis ratio than the finding of Gavazzi (2005) is expected.

Not only does the projected mass increase with the triaxiality, but also does the steepness of the profile. This explains a higher than X-ray derived concentration from the lensing data (§5.4). Although some attempts have been made to model the lensing mass profile with a 3D triaxial halo (Oguri et al. 2005; Corless et al. 2009), no significant constraint on the concentration parameter is obtained (Table 12). To break the degeneracy between the triaxiality and the concentration, observations from different prospective projections, such as X-ray, Sunyaev-Zel'dovich effect, or galaxy kinematics, are always needed.

Riemer-Sørensen et al. (2009) conclude that A1689 harbors a cool core based on the radial temperature profile and a hardness ratio map. From this, they conclude that A1689 is relaxed, excluding the NE half of the cluster, where there is a low mass substructure. Based on the derived temperature profile we disagree that A1689 contains a cool core. The temperature of the cluster varies radially from 9 to 11 keV with a slight drop only after $500 h^{-1}\text{kpc}$. This can not be characterized as the

properties of a cool core cluster. In fact, as shown in Andersson et al. (2009), A1689 is an intermediate stage cluster in terms of central baryon concentration with a minimal core temperature drop. This, does not necessarily provide evidence that the cluster is disturbed but we do not either expect the properties of a cool core cluster. Hardness-ratio maps are very sensitive to accurate background subtraction, especially for high energy splittings. We suspect that the hardness ratio map ($S/H = E[0.3 - 6.0]/E[6.0 - 10.0]$) in Riemer-Sørensen et al. (2009), used as evidence for a cool core, suffers from residual background. The ratio decreases rapidly with radius from a central value of 2.2 and reaches 0.4 already at $3'$. This is an extremely low ratio for any reasonable cluster temperature and it is in disagreement with the observed temperature profile. For comparison, a background-free spectrum from an isothermal cluster at 10 keV would exhibit a count-ratio of ~ 47 in ACIS-I given the energy bands mentioned above. The usage of unsubtracted hardness-ratios in these bands shows that the high-energy band has a significant fractional background contribution and hence, is more spatially flat compared to the low energy band. This does not provide information about the spatial distribution of gas temperatures in the ICM.

7. SUMMARY

We have investigated a deep exposure of Abell 1689 using the ACIS-I instrument aboard the Chandra X-ray telescope. In order to study the discrepancy of the gravitational mass from estimates from gravitational lensing, to that derived using X-ray data, we test the hypothesis of multiple temperature components in projection. The result of a two-temperature model fit shows that it is very important to take into account all details of the calibration of the instrument. We detect an additional absorption feature at 1.75 keV consistent with an absorption edge with an optical depth of 0.13. In analyzing multiple additional datasets, we find similar parameter values for this edge.

If the edge is not modeled, fitting the cluster data within $3'$ strongly favors an additional plasma component at a different temperature. However, when this absorption feature is modeled, the second component does not improve the statistic significantly and the fit results is in better agreement with the XMM MOS data. In all cases, a second component has to have $T > 5$ keV in order for the hot component to agree with the cluster

temperature predicted by Lemze et al. (2008a) which is derived from lensing and S_X profiles. This contradicts the assertion that cool clumps are biasing the X-ray temperature measurements since these substructures would not be cool at all. We also find that, if the temperature profile of the ambient cluster gas is in fact that of Lemze et al. (2008a), the "cool clumps" would have to occupy 70-90% of the space within 250 kpc radius, assuming that the two temperature phases are in pressure equilibrium. In conclusion, we find the scenario proposed by Lemze et al. (2008a) unlikely.

Further studying the ratio of Fe xxvi $K\alpha$ and Fe xxv $K\alpha$ emission lines, we conclude that these show no signs of a multi-temperature projection and the best fit of this ratio implies a single temperature consistent with the continuum temperatures from both *XMM-Newton* MOS and the *Chandra* data when the absorption edge is modeled.

The discrepancy between lensing and X-ray mass estimates remains, particularly in the $r < 200 h^{-1}$ kpc region. Our X-ray mass profile shows consistent results compared to those from weak lensing (e.g., Broadhurst et al. 2005b; Limousin et al. 2007; Umetsu & Broadhurst 2008; Corless et al. 2009). Strong lensing mass profiles from different studies generally give consistent results (e.g., Broadhurst et al. 2005a; Halkola et al. 2006; Limousin et al. 2007), but none of them agrees with those derived from X-ray observations (Xue & Wu 2002; Andersson & Madejski 2004; Riemer-Sørensen et al. 2009). Using a simple ellipsoidal modeling of the cluster with the major axis along the line of sight, we find that the projected mass, as derived from the X-ray analysis, increases by a factor of 1.6 assuming an axis-ratio of 0.6. We conclude that the mass discrepancy between lensing and X-ray derived masses can be alleviated by line of sight ellipticity and that this also can explain the high concentration parameter found in this cluster.

We thank the anonymous referee for valuable suggestions on the manuscript. Support for this work was provided by NASA through SAO Award Number 2834-MIT-SAO-4018 issued by the Chandra X-Ray Observatory Center, which is operated by the Smithsonian Astrophysical Observatory for and on behalf of NASA under contract NAS8-03060. EP sincerely thanks John Arabadjis for his support during early phases of this project.

REFERENCES

- Allen, S. W., Rapetti, D. A., Schmidt, R. W., Ebeling, H., Morris, R. G., & Fabian, A. C. 2008, *MNRAS*, 383, 879
 Allen, S. W., Schmidt, R. W., & Fabian, A. C. 2001, *MNRAS*, 328, L37
 Anders, E., & Grevesse, N. 1989, *Geochim. Cosmochim. Acta*, 53, 197
 Andersson, K., Peterson, J. R., Madejski, G., & Goobar, A. 2009, *ArXiv e-prints*
 Andersson, K. E., & Madejski, G. M. 2004, *ApJ*, 607, 190
 Arabadjis, J. S., Bautz, M. W., & Arabadjis, G. 2004, *ApJ*, 617, 303
 Arnaud, K. A. 1996, in *Astronomical Society of the Pacific Conference Series*, Vol. 101, *Astronomical Data Analysis Software and Systems V*, ed. G. H. Jacoby & J. Barnes, 17–+
- Broadhurst, T., Benítez, N., Coe, D., Sharon, K., Zekser, K., White, R., Ford, H., Bouwens, R., Blakeslee, J., Clampin, M., Cross, N., Franx, M., Frye, B., Hartig, G., Illingworth, G., Infante, L., Menanteau, F., Meurer, G., Postman, M., Ardila, D. R., Bartko, F., Brown, R. A., Burrows, C. J., Cheng, E. S., Feldman, P. D., Golimowski, D. A., Goto, T., Gronwall, C., Herranz, D., Holden, B., Homeier, N., Krist, J. E., Lesser, M. P., Martel, A. R., Miley, G. K., Rosati, P., Sirianni, M., Sparks, W. B., Steindling, S., Tran, H. D., Tsvetanov, Z. I., & Zheng, W. 2005a, *ApJ*, 621, 53
 Broadhurst, T., Takada, M., Umetsu, K., Kong, X., Arimoto, N., Chiba, M., & Futamase, T. 2005b, *ApJ*, 619, L143
 Cavagnolo, K. W., Donahue, M., Voit, G. M., & Sun, M. 2008, *ApJ*, 682, 821
 Cavaliere, A., & Fusco-Femiano, R. 1978, *A&A*, 70, 677
 Comerford, J. M., & Natarajan, P. 2007, *MNRAS*, 379, 190

- Corless, V. L., King, L. J., & Clowe, D. 2009, *MNRAS*, 393, 1235
- Czoske, O. 2004, in *IAU Colloq. 195: Outskirts of Galaxy Clusters: Intense Life in the Suburbs*, ed. A. Diaferio, 183–187
- De Luca, A., & Molendi, S. 2004, *A&A*, 419, 837
- de Plaa, J., Werner, N., Bleeker, J. A. M., Vink, J., Kaastra, J. S., & Méndez, M. 2007, *A&A*, 465, 345
- Dickey, J. M., & Lockman, F. J. 1990, *ARA&A*, 28, 215
- Diego, J. M., Sandvik, H. B., Protopapas, P., Tegmark, M., Benítez, N., & Broadhurst, T. 2005, *MNRAS*, 362, 1247
- Faltenbacher, A., Kravtsov, A. V., Nagai, D., & Gottlöber, S. 2005, *MNRAS*, 358, 139
- Forman, W., Jones, C., Churazov, E., Markevitch, M., Nulsen, P., Vikhlinin, A., Begelman, M., Böhringer, H., Eilek, J., Heinz, S., Kraft, R., Owen, F., & Pahre, M. 2007, *ApJ*, 665, 1057
- Frye, B. L., Coe, D., Bowen, D. V., Benítez, N., Broadhurst, T., Guhathakurta, P., Illingworth, G., Menanteau, F., Sharon, K., Lupton, R., Meylan, G., Zekser, K., Meurer, G., & Hurley, M. 2007, *ApJ*, 665, 921
- Gavazzi, R. 2005, *A&A*, 443, 793
- Halkola, A., Seitz, S., & Pannella, M. 2006, *MNRAS*, 372, 1425
- Hashimoto, Y., Böhringer, H., Henry, J. P., Hasinger, G., & Szokoly, G. 2007, *A&A*, 467, 485
- Hennawi, J. F., Dalal, N., Bode, P., & Ostriker, J. P. 2007, *ApJ*, 654, 714
- Iwamoto, K., Brachwitz, F., Nomoto, K., Kishimoto, N., Umeda, H., Hix, W. R., & Thielemann, F.-K. 1999, *ApJS*, 125, 439
- Jeltema, T. E., Hallman, E. J., Burns, J. O., & Motl, P. M. 2008, *ApJ*, 681, 167
- Kaastra, J. S., & Mewe, R. 2000, in *Atomic Data Needs for X-ray Astronomy*, ed. M. A. Bautista, T. R. Kallman, & A. K. Pradhan, 161–
- Kaastra, J. S., Tamura, T., Peterson, J. R., Bleeker, J. A. M., Ferrigno, C., Kahn, S. M., Paerels, F. B. S., Piffaretti, R., Branduardi-Raymont, G., & Böhringer, H. 2004, *A&A*, 413, 415
- Kawahara, H., Suto, Y., Kitayama, T., Sasaki, S., Shimizu, M., Rasia, E., & Dolag, K. 2007, *ApJ*, 659, 257
- Kotov, O., & Vikhlinin, A. 2005, *ApJ*, 633, 781
- Kravtsov, A. V., Vikhlinin, A., & Nagai, D. 2006, *ApJ*, 650, 128
- Lau, E. T., Kravtsov, A. V., & Nagai, D. 2009, *ArXiv e-prints*
- Leccardi, A., & Molendi, S. 2007, *A&A*, 472, 21
- , 2008, *A&A*, 486, 359
- Lemze, D., Barkana, R., Broadhurst, T. J., & Rephaeli, Y. 2008a, *MNRAS*, 386, 1092
- Lemze, D., Broadhurst, T., Rephaeli, Y., Barkana, R., & Umetsu, K. 2008b, *ArXiv e-prints*
- Limousin, M., Richard, J., Jullo, E., Kneib, J.-P., Fort, B., Soucaill, G., Elíasdóttir, Á., Natarajan, P., Ellis, R. S., Smail, I., Czoske, O., Smith, G. P., Hudelot, P., Bardeau, S., Ebeling, H., Egami, E., & Knudsen, K. K. 2007, *ApJ*, 668, 643
- Lokas, E. L., Prada, F., Wojtak, R., Moles, M., & Gottlöber, S. 2006, *MNRAS*, 366, L26
- Markevitch, M., Bautz, M. W., Biller, B., Butt, Y., Edgar, R., Gaetz, T., Garmire, G., Grant, C. E., Green, P., Juda, M., Plucinsky, P. P., Schwartz, D., Smith, R., Vikhlinin, A., Virani, S., Wargelin, B. J., & Wolk, S. 2003, *ApJ*, 583, 70
- Mathiesen, B. F., & Evrard, A. E. 2001, *ApJ*, 546, 100
- Matsushita, K., Belsole, E., Finoguenov, A., & Böhringer, H. 2002, *A&A*, 386, 77
- Mazzotta, P., Rasia, E., Moscardini, L., & Tormen, G. 2004, *MNRAS*, 354, 10
- Miralda-Escude, J., & Babul, A. 1995, *ApJ*, 449, 18
- Nagai, D., Vikhlinin, A., & Kravtsov, A. V. 2007, *ApJ*, 655, 98
- Navarro, J. F., Frenk, C. S., & White, S. D. M. 1997, *ApJ*, 490, 493
- Neumann, D. M. 2005, *A&A*, 439, 465
- Nevalainen, J., Markevitch, M., & Lumb, D. 2005, *ApJ*, 629, 172
- Oguri, M., & Blandford, R. D. 2009, *MNRAS*, 392, 930
- Oguri, M., Takada, M., Umetsu, K., & Broadhurst, T. 2005, *ApJ*, 632, 841
- Piffaretti, R., Jetzer, P., & Schindler, S. 2003, *A&A*, 398, 41
- Pointecouteau, E., Arnaud, M., Kaastra, J., & de Plaa, J. 2004, *A&A*, 423, 33
- Pratt, G. W., & Arnaud, M. 2002, *A&A*, 394, 375
- Protossov, R., van Dyk, D. A., Connors, A., Kashyap, V. L., & Siemiginowska, A. 2002, *ApJ*, 571, 545
- Rasia, E., Ettori, S., Moscardini, L., Mazzotta, P., Borgani, S., Dolag, K., Tormen, G., Cheng, L. M., & Diaferio, A. 2006, *MNRAS*, 369, 2013
- Riemer-Sørensen, S., Paraficz, D., Ferreira, D. D. M., Pedersen, K., Limousin, M., & Dahle, H. 2009, *ApJ*, 693, 1570
- Saha, P., Williams, L. L. R., & Ferreras, I. 2007, *ApJ*, 663, 29
- Sanders, J. S., & Fabian, A. C. 2002, *MNRAS*, 331, 273
- , 2007, *MNRAS*, 381, 1381
- Sarazin, C. L. 1988, *X-ray emission from clusters of galaxies* (Cambridge Astrophysics Series, Cambridge: Cambridge University Press, 1988)
- Smith, R. K., Brickhouse, N. S., Liedahl, D. A., & Raymond, J. C. 2001, *ApJ*, 556, L91
- Snowden, S. L., Mushotzky, R. F., Kuntz, K. D., & Davis, D. S. 2008, *A&A*, 478, 615
- Tyson, J. A., Wenk, R. A., & Valdes, F. 1990, *ApJ*, 349, L1
- Umetsu, K., & Broadhurst, T. 2008, *ApJ*, 684, 177
- Vikhlinin, A. 2006, *ApJ*, 640, 710
- Vikhlinin, A., Burenin, R. A., Ebeling, H., Forman, W. R., Hornstrup, A., Jones, C., Kravtsov, A. V., Murray, S. S., Nagai, D., Quintana, H., & Voevodkin, A. 2009, *ApJ*, 692, 1033
- Vikhlinin, A., Forman, W., & Jones, C. 1999, *ApJ*, 525, 47
- Vikhlinin, A., Kravtsov, A., Forman, W., Jones, C., Markevitch, M., Murray, S. S., & Van Speybroeck, L. 2006, *ApJ*, 640, 691
- Vikhlinin, A., Markevitch, M., Murray, S. S., Jones, C., Forman, W., & Van Speybroeck, L. 2005, *ApJ*, 628, 655
- Werner, N., Durret, F., Ohashi, T., Schindler, S., & Wiersma, R. P. C. 2008, *Space Science Reviews*, 134, 337
- Xue, S.-J., & Wu, X.-P. 2002, *ApJ*, 576, 152
- Zekser, K. C., White, R. L., Broadhurst, T. J., Benítez, N., Ford, H. C., Illingworth, G. D., Blakeslee, J. P., Postman, M., Jee, M. J., & Coe, D. A. 2006, *ApJ*, 640, 639

APPENDIX

INSTRUMENTAL ABSORPTION IN *CHANDRA* DATA

To see whether the absorption feature found in A1689 (§2.4) is a calibration problem, we analyzed other archived *Chandra* ACIS-I observations. Objects that have high-quality data and are relatively easy to model are pulsar wind nebula G021.5-00.9, elliptical galaxy NGC 4486 (M87), and the Coma cluster. Unfortunately, due to the high galactic absorption in G021.5-00.9, it is not suitable to use those observations to verify the instrumental absorption. Details of the datasets we used are listed in Table 14. These observations have low N_H ($< 3 \times 10^{20} \text{ cm}^{-2}$), low background level ($< 2\%$ in 1.7-2.0 keV band), and high signal-to-noise ratios. Although the central part of M87 has very complex structures produced by the AGN (e.g., Forman et al. 2007), the *XMM-Newton* observation indicates that the intracluster medium is likely to be single-phase in nature outside those regions (Matsushita et al. 2002). We extracted the spectra from $r = 6' - 7.5'$ of M87 and $r < 5'$ of Coma cluster for each ACIS-I chip and fit with an absorbed single-temperature APEC model, multiplied by an absorption edge. The column density was fixed at the Galactic value (Dickey & Lockman 1990). The redshift and all the elemental abundances, except Al, were free to vary. Parameters for this absorption edge are listed in Table 15. For M87 whose emission is dominated by lines, these parameters are sensitive to the choice of the plasma model. Results from the latest MEKAL-based model, SPEX (version 2.0; Kaastra & Mewe 2000), are also shown in Table 15. In general, an absorption at ~ 1.75 keV with an optical depth of 0.1-0.15 is seen in the datasets.

TABLE 14
Chandra OBSERVATION LOG

Name	N_H^a (10^{20}cm^{-2})	z	ObsID	Data Mode	Obs. Date	Exp. (ks)	Background Norm.				Region	f_B^b (%)	S/N^c
							I0	I1	I2	I3			
M87	2.59	0.00423	5826	VFAINT	2005-03-03	125.5	1.03	1.00	1.04	1.07	6'-7.5'	1.5	235
			5827	VFAINT	2005-05-05	154.4	1.10	1.09	1.09	1.13		1.5	262
			6186	VFAINT	2005-01-31	50.7	1.02	1.04	1.04	1.06		1.5	150
			7212	VFAINT	2005-11-14	64.5	1.15	1.15	1.13	1.23		1.7	168
Coma	0.89	0.0231	9714	VFAINT	2008-03-20	29.6	1.32	1.34	1.18	1.43	<5'	1.9	134

^a Dickey & Lockman (1990)

^b Background fraction in 1.7-2.0 keV band.

^c Signal-to-noise ratio in 1.7-2.0 keV band.

TABLE 15
ABSORPTION EDGE PARAMETERS

Name	ObsID	ccd	APEC			SPEX			
			E_{thresh} (keV)	τ	z	E_{thresh} (keV)	τ	z	
M87	5826	0	$1.47^{+0.02}_{-0.02}$	$0.08^{+0.02}_{-0.02}$	$(4.8^{+0.5}_{-0.6}) \times 10^{-3}$	$1.47^{+0.02}_{-0.02}$	$0.10^{+0.02}_{-0.02}$	$(4.0^{+0.7}_{-0.7}) \times 10^{-3}$	
		1	$1.73^{+0.02}_{-0.03}$	$0.07^{+0.02}_{-0.02}$	$(5.1^{+0.5}_{-0.5}) \times 10^{-3}$	$1.70^{+0.02}_{-0.03}$	$0.08^{+0.01}_{-0.02}$	$(4.4^{+0.4}_{-0.4}) \times 10^{-3}$	
		2	$1.75^{+0.01}_{-0.02}$	$0.12^{+0.03}_{-0.02}$	$(12.8^{+0.6}_{-1.0}) \times 10^{-3}$	$1.73^{+0.01}_{-0.02}$	$0.12^{+0.02}_{-0.02}$	$(8.4^{+1.2}_{-0.3}) \times 10^{-3}$	
		3	$1.79^{+0.02}_{-0.02}$	$0.09^{+0.02}_{-0.02}$	$(5.3^{+0.2}_{-0.3}) \times 10^{-3}$	$1.75^{+0.03}_{-0.02}$	$0.08^{+0.02}_{-0.02}$	$(4.5^{+0.2}_{-0.3}) \times 10^{-3}$	
	5827	0	$1.75^{+0.02}_{-0.02}$	$0.11^{+0.03}_{-0.02}$	$(4.9^{+0.8}_{-0.7}) \times 10^{-3}$	$1.72^{+0.02}_{-0.01}$	$0.11^{+0.01}_{-0.02}$	$(3.8^{+1.0}_{-0.8}) \times 10^{-3}$	
		1	$1.73^{+0.02}_{-0.02}$	$0.10^{+0.02}_{-0.02}$	$(5.5^{+0.5}_{-0.5}) \times 10^{-3}$	$1.72^{+0.02}_{-0.02}$	$0.09^{+0.01}_{-0.02}$	$(3.1^{+0.3}_{-0.7}) \times 10^{-3}$	
		2	$1.81^{+0.02}_{-0.02}$	$0.11^{+0.03}_{-0.02}$	$(4.1^{+0.5}_{-0.2}) \times 10^{-3}$	$1.74^{+0.03}_{-0.04}$	$0.08^{+0.02}_{-0.02}$	$(2.4^{+0.3}_{-0.4}) \times 10^{-3}$	
		3	$2.14^{+0.03}_{-0.04}$	$0.06^{+0.02}_{-0.02}$	$(3.8^{+0.5}_{-0.3}) \times 10^{-3}$	$2.13^{+0.04}_{-0.06}$	$0.06^{+0.02}_{-0.02}$	$(2.3^{+0.5}_{-0.3}) \times 10^{-3}$	
	6186	0	$1.72^{+0.06}_{-0.06}$	$0.09^{+0.03}_{-0.05}$	$(4.6^{+0.7}_{-0.6}) \times 10^{-3}$	$1.70^{+0.04}_{-0.04}$	$0.09^{+0.02}_{-0.03}$	$(4.0^{+0.7}_{-0.7}) \times 10^{-3}$	
		1	$1.73^{+0.03}_{-0.04}$	$0.11^{+0.04}_{-0.03}$	$(5.1^{+0.7}_{-0.5}) \times 10^{-3}$	$1.71^{+0.03}_{-0.03}$	$0.11^{+0.03}_{-0.03}$	$(4.4^{+0.8}_{-0.6}) \times 10^{-3}$	
		2	$1.72^{+0.07}_{-0.06}$	$0.11^{+0.05}_{-0.03}$	$(8.2^{+0.5}_{-0.4}) \times 10^{-3}$	$1.66^{+0.03}_{-0.10}$	$0.10^{+0.02}_{-0.02}$	$(7.9^{+0.4}_{-0.7}) \times 10^{-3}$	
		3	$1.74^{+0.03}_{-0.03}$	$0.12^{+0.03}_{-0.03}$	$(8.1^{+0.3}_{-0.4}) \times 10^{-3}$	$1.70^{+0.04}_{-0.03}$	$0.11^{+0.03}_{-0.03}$	$(7.8^{+0.3}_{-0.3}) \times 10^{-3}$	
7212	0	$1.77^{+0.03}_{-0.02}$	$0.11^{+0.02}_{-0.04}$	$(4.3^{+0.8}_{-0.6}) \times 10^{-3}$	$1.62^{+0.09}_{-1.62}$	$0.08^{+0.02}_{-0.03}$	$(1.0^{+3.4}_{-1.0}) \times 10^{-3}$		
	1	$1.91^{+0.21}_{-0.05}$	$0.10^{+0.04}_{-0.04}$	$(5.8^{+0.4}_{-0.3}) \times 10^{-3}$	$2.00^{+0.04}_{-0.04}$	$0.10^{+0.03}_{-0.05}$	$(2.0^{+0.4}_{-0.4}) \times 10^{-3}$		
		2	1.74_f	$0.01^{+0.03}_{-0.01}$	$(6.4^{+0.5}_{-0.7}) \times 10^{-3}$	1.74_f	$0.02^{+0.03}_{-0.02}$	$(1.2^{+1.0}_{-1.0}) \times 10^{-3}$	
Coma	9714	0	$1.76^{+0.03}_{-0.02}$	$0.14^{+0.06}_{-0.02}$	$(4.6^{+0.9}_{-0.2}) \times 10^{-2}$	$1.76^{+0.03}_{-0.02}$	$0.15^{+0.04}_{-0.05}$	$(4.6^{+0.8}_{-0.2}) \times 10^{-2}$	
		1	$1.75^{+0.05}_{-0.05}$	$0.08^{+0.04}_{-0.05}$	$(3.1^{+0.5}_{-0.6}) \times 10^{-2}$	$1.75^{+0.05}_{-0.05}$	$0.08^{+0.03}_{-0.05}$	$(2.6^{+0.8}_{-0.4}) \times 10^{-2}$	
		2	$1.75^{+0.02}_{-0.02}$	$0.11^{+0.04}_{-0.02}$	$(3.2^{+0.7}_{-0.3}) \times 10^{-2}$	$1.75^{+0.03}_{-0.03}$	$0.10^{+0.05}_{-0.02}$	$(3.2^{+0.6}_{-0.4}) \times 10^{-2}$	
		3	$1.77^{+0.02}_{-0.02}$	$0.18^{+0.03}_{-0.03}$	$(3.8^{+0.2}_{-0.4}) \times 10^{-2}$	$1.77^{+0.02}_{-0.02}$	$0.17^{+0.03}_{-0.03}$	$(3.7^{+0.3}_{-0.5}) \times 10^{-2}$	
		3	$1.75^{+0.06}_{-0.06}$	$0.03^{+0.03}_{-0.02}$	$(4.8^{+0.5}_{-0.5}) \times 10^{-3}$	$1.73^{+0.05}_{-0.09}$	$0.03^{+0.02}_{-0.01}$	$(2.3^{+0.3}_{-0.8}) \times 10^{-3}$	
A1689	540	13	$1.72^{+0.05}_{-0.03}$	$0.10^{+0.03}_{-0.04}$	$0.190^{+0.002}_{-0.002}$	$1.72^{+0.05}_{-0.04}$	$0.09^{+0.03}_{-0.03}$	$0.189^{+0.004}_{-0.003}$	
		1663	3	$1.75^{+0.04}_{-0.03}$	$0.16^{+0.04}_{-0.03}$	$0.191^{+0.002}_{-0.011}$	$1.75^{+0.04}_{-0.03}$	$0.16^{+0.04}_{-0.04}$	$0.192^{+0.005}_{-0.012}$
		5004	3	$1.76^{+0.04}_{-0.03}$	$0.15^{+0.02}_{-0.03}$	$0.182^{+0.002}_{-0.005}$	$1.76^{+0.03}_{-0.03}$	$0.15^{+0.03}_{-0.03}$	$0.180^{+0.003}_{-0.003}$
		6930	3	$1.74^{+0.01}_{-0.02}$	$0.12^{+0.01}_{-0.01}$	$0.188^{+0.003}_{-0.003}$	$1.75^{+0.01}_{-0.01}$	$0.12^{+0.01}_{-0.01}$	$0.188^{+0.002}_{-0.002}$
		7289	3	$1.73^{+0.02}_{-0.02}$	$0.14^{+0.01}_{-0.02}$	$0.183^{+0.002}_{-0.003}$	$1.73^{+0.02}_{-0.02}$	$0.13^{+0.01}_{-0.01}$	$0.181^{+0.003}_{-0.003}$

However, for ObsID 7212, the absorption depth is determined less than 0.05 (1σ) on ACIS-I2 and I3.